*J. Fluid Mech.* (1997), *vol.* 351, *pp.* 167–199. Printed in the United Kingdom

# Properties of the mean recirculation region in the wakes of two-dimensional bluff bodies

By S. BALACHANDAR,[1] R. MITTAL[1] AND F. M. NAJJAR[2]

[1] Department of Theoretical and Applied Mechanics, University of Illinois at Urbana–Champaign, 104 South Wright Street, Urbana, IL 61801, USA

[2] National Center for Supercomputing Applications, University of Illinois at Urbana–Champaign, Urbana, IL 61801, USA

(Received 12 November 1996 and in revised form 18 July 1997)

The properties of the time- and span-averaged mean wake recirculation region are investigated in separated flows over several different two-dimensional bluff bodies. Ten different cases are considered and they divide into two groups: cylindrical geometries of circular, elliptic and square cross-sections and the normal plate. A wide Reynolds number range from 250 to 140000 is considered, but in all the cases the attached portion of the boundary layer remains laminar until separation. The lower Reynolds number data are from direct numerical simulations, while the data at the higher Reynolds number are obtained from large-eddy simulation and the experimental work of Cantwell & Coles (1983), Krothapalli (1996, personal communication), Leder (1991) and Lyn *et al.* (1995). Unlike supersonic and subsonic separations with a splitter plate in the wake, in all the cases considered here there is strong interaction between the shear layers resulting in Kármán vortex shedding. The impact of this fundamental difference on the distribution of Reynolds stress components and pressure in relation to the mean wake recirculation region (wake bubble) is considered. It is observed that in all cases the contribution from Reynolds normal stress to the force balance of the wake bubble is significant. In fact, in the cylinder geometries this contribution can outweigh the net force from the shear stress, so that the net pressure force tends to push the bubble away from the body. In contrast, in the case of normal plate, owing to the longer wake, the net contribution from shear stress outweighs that from the normal stress. At higher Reynolds numbers, separation of the Reynolds stress components into incoherent contributions provides more insight. The behaviour of the coherent contribution, arising from the dominant vortex shedding, is similar to that at lower Reynolds numbers. The incoherent contribution to Reynolds stress, arising from small-scale activity, is compared with that of a canonical free shear layer. Based on these observations a simple extension of the wake model (Sychev 1982; Roshko 1993*a*, *b*) is proposed.

## 1. Introduction

The problem of the wake behind bluff bodies has been the subject of active scientific investigation for more than a century. Owing to the complex nature of the problem, only a few comprehensive theories have been put forth in the past and these have enjoyed only limited success. One such theory, the free-streamline theory, dates back more than a hundred years to Kirchhoff (1869), who considered the inviscid potential flow past a bluff flat plate with an infinitely long wake at constant pressure equal to the free-stream pressure. This simple theory was able to capture many essential features of separated flow over bluff bodies, but its prediction of drag coefficient, which for the case of a bluff flat plate is 0.88, was significantly lower than actual measurements. This lower prediction is due to the fact that unlike the infinitely long wake assumed in Kirchhoff's theory, the actual wake closes on itself and is finite in length. Correspondingly the actual base pressure is significantly lower than the free-stream pressure. Several improvements to the original theory have been proposed by Riabouchinsky (1920), Roshko (1954), Wu (1962), Batchelor (1956) and Lighthill (1945). All these models allow for the possibility of a base pressure different from and lower than the free-stream pressure. Although the value of the base pressure cannot be determined independently based on free-streamline theory alone, it serves as an adjustable parameter. With an optimal choice for this parameter, these models successfully predict the pressure distribution on the upstream side of the body and provide acceptable predictions for the overall forces. Some of these models, which also account for the finite size of the mean recirculation region in the wake (also referred to as the mean wake bubble), relate the length and width to the base pressure. Although these theories are generally obtained for a steady two-dimensional wake, they apply equally well in the case of an unsteady three-dimensional wake, to the time- and span-averaged properties of the wake and global quantities such as the mean lift and drag coefficients. A thorough review of the free-streamline theories has been given by Wu (1972).

In the past the prediction of base pressure has played a central role in wake modelling. Chapman, Kuehn & Larson (1957) and Korst (1956) have independently developed theories for base pressure prediction, primarily for supersonic flow. The essential idea in both these theories is that the base pressure or the dead-air pressure in the wake is calculated by equating the total pressure along the dividing streamline to the static pressure downstream. The Reynolds and Mach number dependence of the base pressure predicted by this simple theory has been well confirmed by experimental results on various bluff bodies over a range of Reynolds and supersonic Mach numbers. The main restricting assumptions made in this theory are that the compression along the dividing streamline in the reattachment region is isentropic and that additional pressure increase downstream of the reattachment point is neglected in the theory. Furthermore, the Chapman–Korst theory is strictly valid only in the limit of very small thickness of the separating shear layer compared to the dimensions of the wake. Nash (1963) suggests an extension to the Chapman–Korst theory which takes into account the influence of the finite thickness of the shear layer at separation and the difference in pressure at reattachment from the final recovery pressure far downstream. Further modifications to the Chapman–Korst theory have been proposed by Roberts (1966), Carrière & Sirieix (1960) and Tanner (1973).

It is to be noted that in the case of supersonic separation, the periodic vortex shedding mechanism, commonly observed at subsonic velocities, is largely suppressed. This is an essential feature, since in the development of the above theories, the separated shear layer is assumed to be steady and two-dimensional. Therefore, Chapman *et al.* (1957) applied this theory to subsonic (and incompressible) separated flows only when vortex shedding is suppressed, which can be accomplished by placing a splitter plate in the wake of the bluff body. Roshko & Lau (1965) measured pressure along the splitter plate in the wake of various bluff-body geometries at subsonic speeds and pointed out that the problem with the application of the Chapman–Korst theory to subsonic flows is in the appropriate definition of the downstream pressure. Instead of the standard pressure coefficient, Roshko & Lau (1965) defined a reduced pressure-rise coefficient, which when plotted against the distance from the base normalized by the length of the wake recirculation region, brilliantly collapsed the data as long as the shear layer thickness at separation is small. They showed that the reduced pressure-rise coefficient recovers uniformly for a variety of configurations to an asymptotic value of 0.35 while it is approximately 0.27 at the reattachment point. However, despite its success in collapsing the data, this approach does not provide a way to determine the base pressure independently.

Following Sychev (1982), Roshko (1993*a*, *b*) put forth a different approach for the closure of the bluff-body wake problem. This model considers the equilibrium of the mean wake recirculation region and a balance of force between the shear stress acting along the top and bottom of the mean wake and the net pressure force. At sufficiently large Reynolds numbers the viscous contribution to the shear stress is negligible and with an empirical input for the best estimate of Reynolds shear stress, this approach results in a relation between the length and width of the wake recirculation region and the pressure difference between the base and the reattachment point. The free-streamline theory provides the second relation between the dimensions of the wake and the base pressure. By requiring that these two relations be simultaneously satisfied, Roshko (1993*a*) was able to obtain theoretical estimates of base pressure and drag coefficient for a normal plate with a splitter plate in the wake and these were found to compare well with the experimental results of Arie & Rouse (1956) and Castro & Haque (1987). Roshko (1993*a*, *b*) limited this analysis to wakes without vortex shedding and suggested a possible universal description in this case. He clearly pointed out problems that arise in extending this model to subsonic wakes with strong vortex shedding. The main hurdle seems to be the lack of reliable experimental data on pressure and Reynolds stress components in the near-wake region. For example, pressure measurements in the wake without interfering with the flow are in general difficult. Furthermore, accurate measurement of Reynolds stresses in the near-wake region is challenging, since the size of the mean wake recirculation region decreases significantly in the presence of vortex shedding.

In the present study we focus on an extension of the approach suggested by Sychev (1982) and Roshko (1993*a*, *b*) to incompressible bluff-body wakes with strong shear layer interaction and vortex shedding. We investigate the distributions of pressure and Reynolds stresses and study the balance of forces within the time- and span-averaged mean wake recirculation region. Four different geometries, namely circular, elliptic, and square cylinders and a normal flat plate without a splitter plate in the wake, will be considered. Direct numerical simulation (DNS) and large-eddy simulation (LES) databases will be used to compute the pressure and Reynolds stress distributions in the wake recirculation region. A significant limitation of the above simulations is that they cover only a limited Reynolds number range from 250 to 4000. Therefore we have also considered the experimental measurements of Cantwell & Coles (1983) and A. Krothapalli (1996, personal communication) of the wake behind a circular cylinder at $Re = 140\,000$ and $Re = 3000$, respectively, of Lyn *et al.* (1995) over a square cylinder at $Re = 21\,400$ and of Leder (1991) for the flow around a normal flat plate at $Re = 28\,000$. These experiments allow us to obtain high-Reynolds-number results for the distribution of Reynolds stresses around the wake bubble. It was observed that the computational results on the Reynolds stress distribution qualitatively agree with those measured in the high-Reynolds-number experiments. Unfortunately, the computed pressure distribution in the near-wake region could not be verified at higher Reynolds numbers for lack of experimental measurements.

Based on the results, we observe that with the presence of vortex shedding and strong interaction between the separated shear layers, the contribution from the Reynolds streamwise normal stress component to the streamwise force balance of the wake is not negligible. In fact, for the case of circular, elliptic and square cylinders, the net force from the Reynolds streamwise normal stress outweighs the net force from the Reynolds shear stress, so that the net pressure force on the wake bubble tends to push it away from the body. Thus the streamwise forces due to pressure and shear stress act along the same direction and do not balance each other.

The importance of transition location relative to the separation and reattachment points has been well recognized in wakes both with (Roshko & Fiszdon 1969) and without vortex shedding (Chapman *et al.* 1957). At low Reynolds numbers, for $Re \lesssim 190$ in the case of a circular cylinder, the near-wake vortex shedding is laminar. With increasing Reynolds number, three-dimensional instabilities appear and the wake becomes transitional (Williamson 1996). In these early regimes the Reynolds stress in and around the mean wake recirculation region is primarily due to the time-dependent nature of vortex shedding. In this limit, it is observed that the Reynolds shear stress is relatively small along the periphery and the Reynolds normal stress is in approximate balance with the pressure force. At very low Reynolds numbers, viscous stresses begin to play a role as well. At higher Reynolds numbers, for $10^3 \lesssim Re \lesssim 2 \times 10^5$ in the case of a circular cylinder, the separated shear layers become unstable and the point of instability moves progressively upstream towards the separation point with increasing Reynolds number. At even higher Reynolds numbers the transition point moves up into the attached boundary layers (Williamson 1996). In these shear layer transition and boundary layer transition regimes, the Reynolds stress distribution can be conveniently split into a coherent contribution arising from vortex shedding and an incoherent contribution arising from the turbulent fluctuations, as shown by Reynolds & Hussain (1972) and Cantwell & Coles (1983). At these high Reynolds numbers, the coherent part of the Reynolds shear stress arising from vortex shedding is negligible along the periphery of the mean wake bubble. However, the incoherent contribution to Reynolds shear stress along the periphery is not negligible and increases in magnitude with Reynolds number.

Furthermore, the above observations on the distribution of Reynolds normal and shear stresses around the wake are in general found to be true even for the case of a normal flat plate. The contribution to the force balance from the normal stress is significant and that from the coherent component of the shear stress is small. In contrast to the circular cylinder even at relatively low Reynolds numbers when transition is limited to the wake, the contribution to Reynolds shear stress from the incoherent part is seen to be significant. The underlying cause for this is the low-frequency oscillation of the near-wake region (Roshko 1993*a*; Lyn & Rodi 1994; Najjar 1994), which is quite pronounced for flow past a normal plate. In addition, the wake length is significantly longer and the net streamwise force arising from the shear stress outweighs that from the normal stress. Thus the streamwise pressure force is against the free-stream flow direction, similar to wakes without vortex shedding. These differences between the cylinder and normal-flat-plate geometries suggest that by controlling the dynamics of the separating shear layers, possibly in terms of the thickness of the separating boundary layer, the shape of the bluff body can play an important role in determining the Reynolds stress distribution and the force balance within the wake (Roshko & Lau 1965; Tanner 1973). In order to explore further the difference in the Reynolds stress distribution between the cylinder and normal-plate geometries, we will examine the dynamics of the near-wake spanwise vortical structures for these two types of bluff bodies and observe their relation to the character of the mean wake and Reynolds stress distribution.

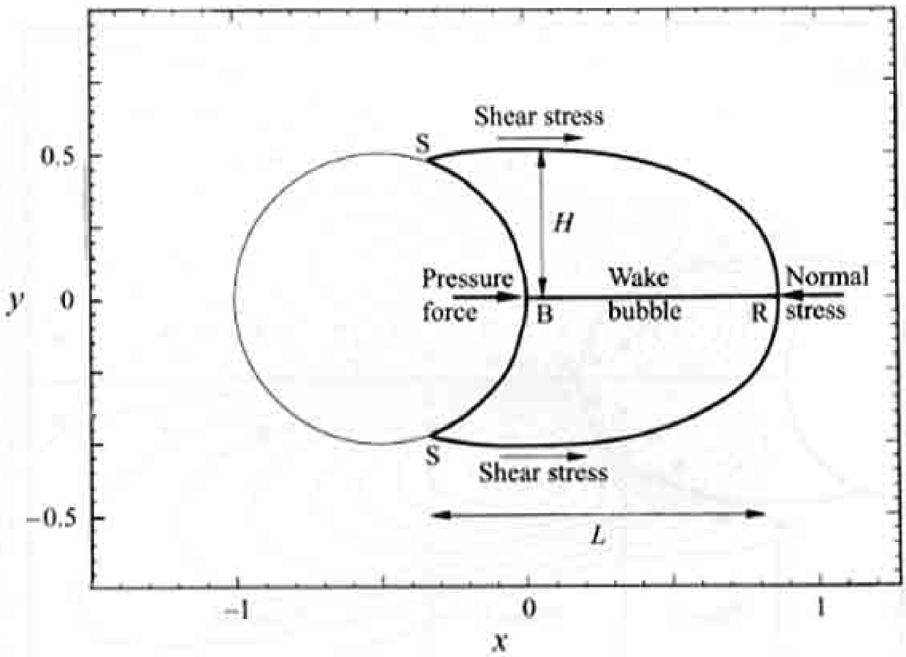

FIGURE 1. Schematic showing the force balance on the mean separation bubble in the wake of a circular cylinder. The base, separation points and the reattachment point at the end of the recirculation zone are marked by B, S and R respectively.

| Case | Bluff body | $Re$ | Methodology | Investigator |
|---|---|---|---|---|
| 1 | Circular cylinder | 300 | DNS | Present study |
| 2 | Circular cylinder | 525 | DNS | Mittal & Balachandar (1995*a*) |
| 3 | Elliptic cylinder<br>0° AOA, 1:2 aspect | 525 | DNS | Mittal & Balachandar (1995*a*) |
| 4 | Circular cylinder | 3000 | PIV | A. Krothapalli (1996, personal communication) |
| 5 | Circular cylinder | 3900 | LES | Mittal (1996) |
| 6 | Circular cylinder | 140000 | Flying hotwire | Cantwell & Coles (1983) |
| 7 | Square cylinder | 21400 | LDV | Lyn *et al.* (1995) |
| 8 | Normal flat plate | 250 | DNS | Present study |
| 9 | Normal flat plate | 1000 | DNS | Najjar & Vanka (1995) |
| 10 | Normal flat plate | 28000 | PIV | Leder (1991) |

TABLE 1. Details on the 10 different cases considered including the Reynolds number, methodology and the source of the data

The rest of the paper will be organized as follows: §2 will present a simple force balance around the mean wake recirculation region and appropriate pressure and stress coefficients will be defined. The results for a circular cylinder at $Re = 300$ will be presented first in §3.1, followed by results for other cylindrical bluff bodies in §3.2. Coherent and incoherent contributions to Reynolds stress components will be separated and analysed in §3.3. Results for the normal plate will be presented in §3.4. In §3.5 the relation between Kármán vortex dynamics and the shape and size of the mean wake as well as the contribution of the coherent contribution to Reynolds stress will be discussed. Finally a discussion of results and conclusions will be presented in §4.

## 2. Force balance for the mean wake recirculation region

Here we follow Sychev (1982) and Roshko (1993*a*, *b*) and consider the balance of streamwise forces acting on a mean wake recirculation region. Figure 1 shows a schematic of the mean wake with forces acting on it. The length of the wake, $L$, is

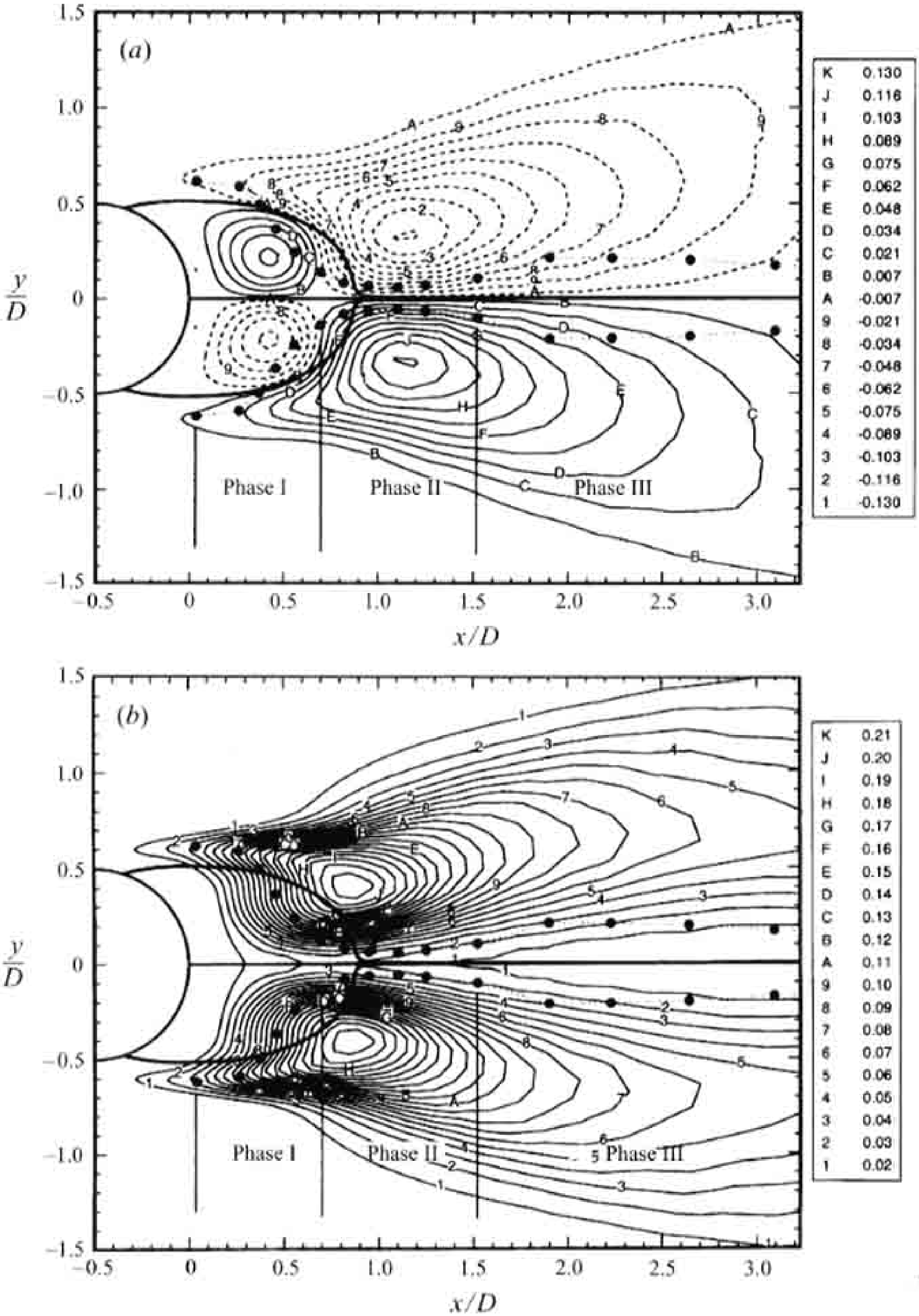

FIGURE 2 (*a*, *b*). For caption see facing page.

defined as the streamwise distance from the separation point (marked S) to the reattachment point (marked R) and the half-height is denoted by $H$ and it is measured at the thickest point of the mean wake. Since we consider here a time-dependent and possibly three-dimensional separated flow, the top and bottom boundaries of the mean wake recirculation region are given by the separating streamlines of the time- and span-averaged flow field. Hence the force balance will also be considered in the time- and span-averaged sense. From the definition of the separating streamline there is no net

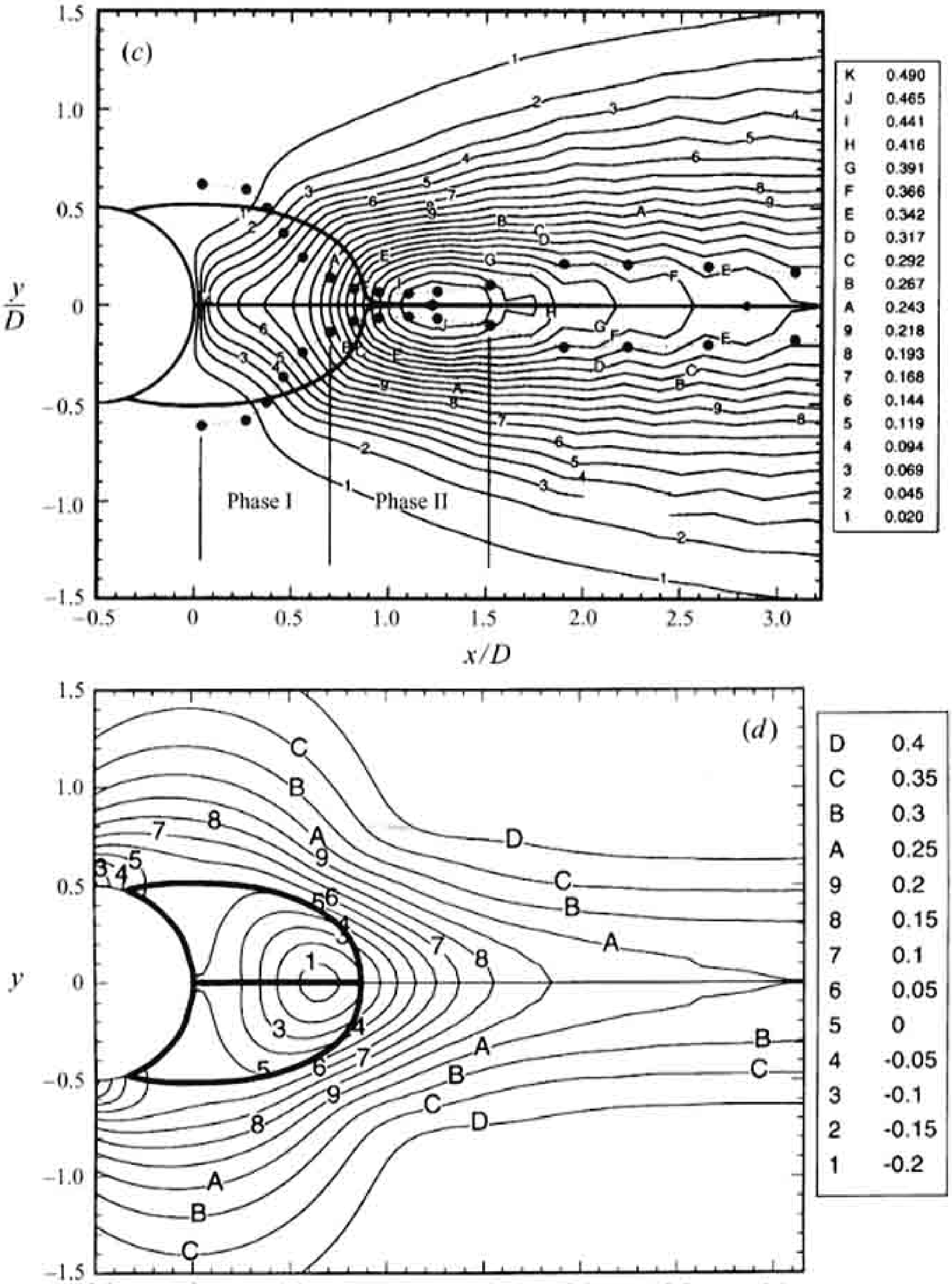

FIGURE 2. Coherent Reynolds stress and pressure distribution in the wake of a circular cylinder at a Reynolds number of 300. The Reynolds stresses are non-dimensionalized with respect to $U_\infty^2$. Solid and dashed lines denote positive and negative values respectively. The mean separation streamline is shown by a thick line. The dotted line connecting the filled dots represents the trajectory of the spanwise Kármán vortices as they form in the near wake and convect downstream. Each circular symbol marks the position of the vortices after 1/10 of the shedding period. The three phases in the vortex trajectory have also been marked. (*a*) Reynolds shear stress, (*b*) Reynolds streamwise normal stress, (*c*) Reynolds cross-stream normal stress and (*d*) pressure coefficient.

flow through the boundary of the recirculation region. Thus the streamwise momentum balance for the fluid inside the wake bubble can be expressed as

$$\int_{\partial\Omega} \bar{p} n_1 \,\mathrm{d}s + \int_{\partial\Omega} \left( \overline{u'^2} - \frac{1}{Re} \frac{\partial \bar{u}}{\partial x} \right) n_1 \,\mathrm{d}s = - \int_{\partial\Omega} \left( \overline{u'v'} - \frac{1}{Re} \frac{\partial \bar{u}}{\partial y} \right) n_2 \,\mathrm{d}s \tag{1}$$

where $\partial\Omega$ represents the boundary of the wake bubble and $n_1$ and $n_2$ are the direction cosines of the outward unit normal to the boundary, $\partial\Omega$. In the above equation velocity is non-dimensionalized by the free-stream velocity $U_\infty$, length is non-dimensionalized by a suitably chosen diameter $D$ of the bluff body, and therefore Reynolds number is defined as $Re = U_\infty D/\nu$. The pressure and Reynolds stress components are accordingly non-dimensionalized by $\rho U_\infty^2$ and $U_\infty^2$. In (1) $\bar{u}$ and $\bar{p}$ are the time- and span-averaged non-dimensional streamwise velocity and pressure, and $\overline{u'^2}$ and $\overline{u'v'}$ are the corresponding non-dimensional Reynolds streamwise normal and shear stresses. The term on the right-hand side of (1) accounts for the net $x$ force due to Reynolds and viscous shear stresses. The two terms on the left account for the net pressure force and force due to the Reynolds and viscous streamwise normal stresses, acting along the negative $x$-direction. For completeness, forces due to the viscous stresses were also included in (1). However, in the subsequent analysis, the viscous stresses will be ignored since their contribution is expected to be small at high Reynolds numbers. Following Roshko (1993*b*) the pressure, normal and shear stress coefficients are defined as follows:

$$C_p = \frac{\bar{p} - \overline{p_b}}{\frac{1}{2} U_e^2}, \quad C_n = \frac{\overline{u'^2}}{\frac{1}{2} U_e^2}, \quad C_\tau = -\frac{\overline{u'v'}}{\frac{1}{2} U_e^2} \tag{2}$$

where $\overline{p_b}$ is the mean non-dimensional pressure at the base of the model and $U_e$ is the non-dimensional velocity at the edge of the separated shear layer on the high-speed side. In terms of these pressure and stress coefficients the approximate streamwise force balance, neglecting the viscous contribution, can be written as

$$\int_{\partial\Omega} C_p n_1 \,\mathrm{d}s + \int_{\partial\Omega} C_n n_1 \,\mathrm{d}s = \int_{\partial\Omega} C_\tau n_2 \,\mathrm{d}s. \tag{3}$$

The net contribution to the streamwise force balance from the pressure and Reynolds normal and shear stresses can be defined as follows:

$$[C_p] = \int_{\partial\Omega} C_p n_1 \,\mathrm{d}s, \quad [C_n] = \int_{\partial\Omega} C_n n_1 \,\mathrm{d}s, \quad [C_\tau] = \int_{\partial\Omega} C_\tau n_2 \,\mathrm{d}s. \tag{4}$$

In the following section the distribution of pressure and Reynolds stress coefficients around the wake and their net contribution to streamwise force balance will be considered for several canonical bluff-body geometries over a range of Reynolds numbers.

## 3. Results

In the present study results obtained from a total of 10 different cases will be considered. The two primary bluff bodies considered are a circular cylinder and a flat plate held normal to the flow. Both these geometries are considered over a range of Reynolds numbers. Additional results are provided for cylinders of elliptic and square cross-sections. Detailed pressure and Reynolds stress distributions for six of the cases are obtained from direct and large-eddy simulations. Owing to resolution requirements, the Reynolds numbers for these numerical simulations are generally low, ranging from 250 to 3900. Therefore, the detailed experimental Reynolds stress measurements of four other high-Reynolds-number cases are also analysed. Table 1 summarizes the

| Cross-section | $L/D$ | $H/D$ | $L/H$ | $U_s$ | $Re^*$ |
|---|---|---|---|---|---|
| Circular cylinder $Re = 300$ | 1.21 | 0.51 | 2.37 | 1.360 | 416 |
| Circular cylinder $Re = 525$ | 1.19 | 0.52 | 2.29 | 1.388 | 758 |
| Elliptic cylinder $Re = 525$ | 1.98 | 0.50 | 3.96 | 1.245 | 654 |
| Circular cylinder $Re = 3000$† | 1.768 | 0.635 | 2.78 | 1.54 | 5867 |
| Circular cylinder $Re = 3900$ | 1.99 | 0.60 | 3.32 | 1.350 | 6318 |
| Circular cylinder $Re = 140000$†† | 1.10 | 0.55 | 2.00 | 1.36 | 209440 |
| Square cylinder $Re = 21400$‡ | 1.88 | 0.74 | 2.54 | 1.445 | 45766 |
| Normal plate $Re = 250$ | 2.35 | 0.80 | 2.93 | 1.450 | 580 |
| Normal plate $Re = 1000$ | 2.55 | 0.854 | 2.98 | 1.488 | 2542 |
| Normal plate $Re = 28000$§ | 2.50 | 0.82 | 3.05 | 1.35 | 61992 |

TABLE 2. Geometrical properties and high-speed velocity of the separating shear layer for the different cases. † A. Krothapalli, personal communication (1996), †† Cantwell & Coles (1983), ‡ Lyn *et al.* (1995) and § Leder (1991).

various cases considered and also provides the sources for these different experimental and computational data. The direct numerical simulation data for the circular and elliptic cylinders at $Re = 525$ are the same as those described and used in Mittal & Balachandar (1995*a*, *b*). The large-eddy simulation of flow over a circular cylinder at $Re = 3900$ has been addressed in Mittal (1996). The computational details and flow statistics for the normal flat plate at $Re = 1000$ have been presented in Najjar & Vanka (1995). The low-Reynolds-number simulation results of the circular cylinder at $Re = 300$ and the normal flat plate at $Re = 250$ are particular to the present study. Therefore, essential computational details on these cases alone will be presented.

### 3.1. *Circular cylinder at Re = 300*

We first present results for the canonical problem of flow over a circular cylinder at a Reynolds number of 300, based on cylinder diameter. A Fourier–Chebyshev spectral collocation method (Canuto *et al.* 1988) is used to simulate the flow in a body-fitted elliptic cylindrical grid. The circumferential direction ($\theta$) is intrinsically periodic and a Fourier expansion is used in this direction. An appropriate spanwise length, $L_z$, is chosen for the simulation and the flow is assumed to be periodic in the spanwise direction ($z$). This allows for the use of Fourier collocation along this direction. For this particular simulation, $L_z = 1.8D$, which is appoximately twice the spanwise wavelength of the dominant mode B three-dimensional instability (Williamson 1996) and therefore allows for two pairs of streamwise ribs in the spanwise direction. The wall-normal direction ($r$) is non-periodic and therefore a Chebyshev expansion is used for discretization. The infinite flow domain is truncated to a finite extent ($15D$ in this case) in the radial direction and non-reflecting boundary conditions are applied at the outflow boundary. Furthermore, a mixed boundary condition is applied at the inflow boundary which allows the incoming uniform flow to adjust to the displacement effect

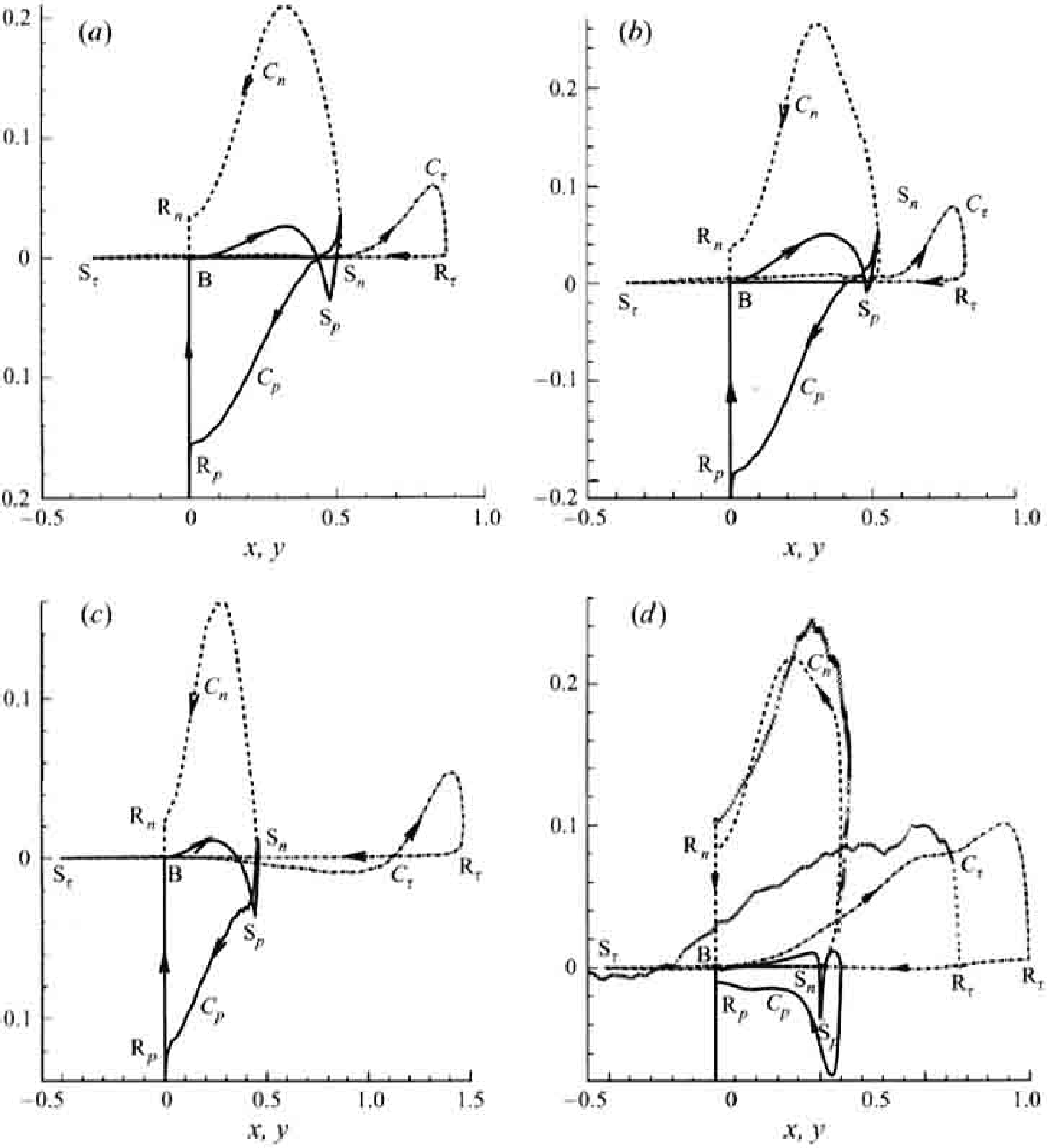

FIGURE 3(a–d). For caption see facing page.

of the body. An 81 × 160 × 72 ($r \times \theta \times z$) mesh is used and the solution has been shown to be independent of the grid and radial domain size (Mittal & Balachandar 1997). A two-step time-split method is employed to advance the solution in time through the advection–diffusion and pressure-correction steps. A homogeneous Neumann pressure boundary condition is used on the body in conjunction with a higher-order intermediate velocity boundary condition. These boundary conditions satisfy no penetration exactly and no slip to $O(\Delta t^3)$ accuracy on the cylinder surface where $\Delta t$ is the time-step size. Further details of the numerical method can be found in Mittal & Balachandar (1996) and Mittal (1995). The simulation predicts a mean drag coefficient and base suction pressure coefficient of 1.27 and 1.04 respectively, which are slightly higher than the corresponding experimental values of 1.22 (Wieselsberger 1922) and 0.96 (Williamson 1996). The predicted Strouhal number is 0.207 which is in good agreement with the experimental value of 0.203 (Williamson 1996). It should be pointed out that at this modest Reynolds number of 300, the flow is three-dimensional and time-dependent but is dominated by the primary Strouhal frequency.

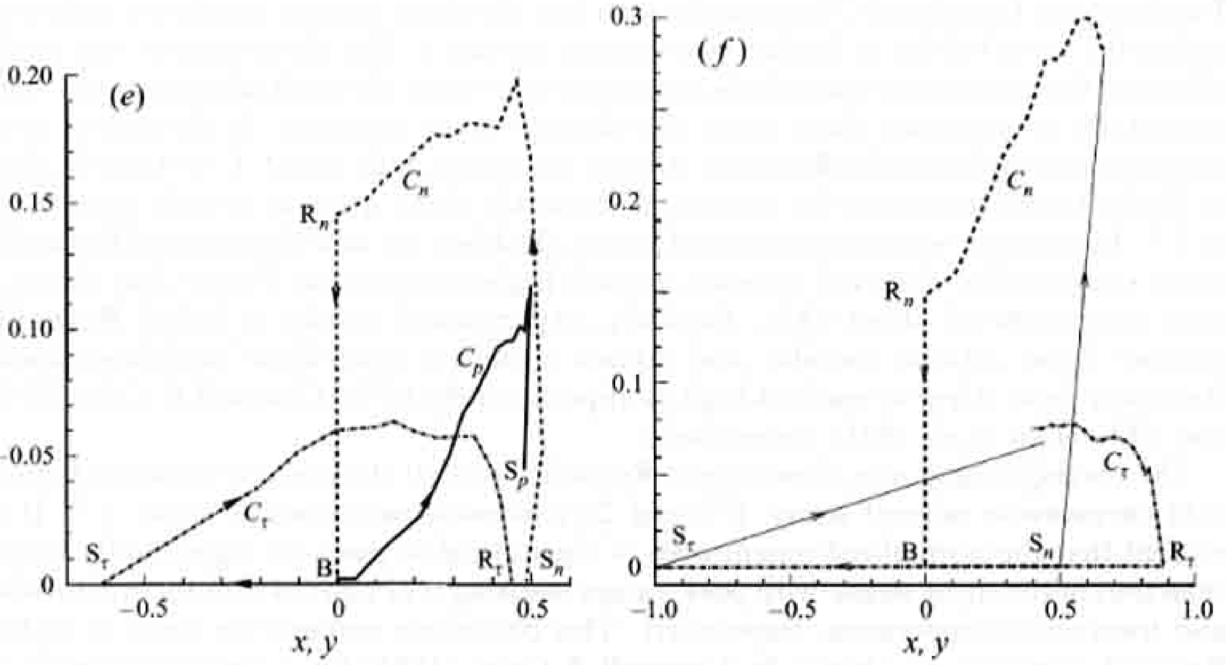

FIGURE 3. Variation of computed mean pressure and stress coefficients ($C_p$, $C_n$ and $C_\tau$) along the periphery of the mean wake recirculation region. The pressure, shear stress and the streamwise normal stress coefficients are shown by solid, dash–dot and dashed lines respectively. Owing to the symmetry of the mean wake about the wake centreline ($y = 0$), these coefficients will only be presented over the upper half of the wake. The locations of the base (B), separation (S) and reattachment (R) points are marked along each of the closed loops with appropriate subscript $p$, $n$ or $\tau$. Here, $C_p$ and $C_n$ are plotted against $y$ around the bubble, so $y$ ranges from 0 to approximately 0.5, whereas $C_\tau$ is plotted against $x$ around the mean wake bubble. Therefore, the areas enclosed by the closed curves provide the respective integrated $x$-force around the mean separation bubble. A clockwise loop for shear stress corresponds to a positive $[C_\tau]$ with a net force due to shear stress along the flow (or postive $x$) direction. An anticlockwise loop corresponds to positive $[C_p]$ and $[C_n]$ resulting in corresponding pressure and normal stress forces opposite to the flow direction (or along the negative $x$-direction). (*a*) Circular cylinder at $Re = 300$, (*b*) circular cylinder at $Re = 525$, (*c*) an elliptic cylinder at $Re = 525$, (*d*) a circular cylinder at $Re = 3900$. Also plotted on (*d*) are the stress coefficients evaluated from the experimental measurements of A. Krothapalli (1996, personal communication) at $Re = 3000$. Here lines correspond to computational result (solid, $C_p$; dashed, $C_n$; dashed–dot, $C_\tau$) and symbols correspond to experimental results (×, $C_n$; +, $C_\tau$). (*e*) The experimental results of Cantwell & Coles (1983) for a circular cylinder at $Re = 140000$. Pressure coefficient is plotted only along the leeward side of the cylinder from the base to the separation point. (*f*) The experimental results of Lyn *et al.* (1995) for a square cylinder at $Re = 21400$.

Figure 2(*a*) shows the non-dimensional Reynolds shear stress, $\overline{u'v'}$, distribution (non-dimensionalization is with $U_\infty^2$). Also plotted are the separating streamlines of the mean flow so that the correspondence between the Reynolds shear stress and the mean wake recirculation region can be seen. The circular symbols denote the trajectory of the Kármán vortices and this will be discussed in §3.5. The non-dimensional wake length ($L/D$) measured from the separation to the reattachment point can be seen to be approximately 1.21 and the corresponding non-dimensional half-height of the wake ($H/D$) is 0.51. The length, width and some other properties of the mean wake bubble are listed in table 2 for all the cases considered. In comparison, when vortex shedding is inhibited with a splitter plate the resulting mean wake is significantly longer. For example, in the case of a normal plate with a splitter in the wake Arie & Rouse (1956) have measured the length of the mean wake recirculation region to extend up to 4.15 times the height of the normal plate and the resulting length-to-width aspect ratio to be approximately 3.1. Similar results have been obtained as well for the case of circular cylinders where shedding has been inhibited (Nishioka & Sato 1978; Fornberg 1980).

Furthermore, from figure 2(*a*) it can be seen that the shear stress is significant only well within the wake bubble or farther downstream outside it. The shear stress is very small all along the separating streamlines, except perhaps near the reattachment point. The magnitude of maximum shear stress also deserves some attention. In the case of non-interacting shear layers the Reynolds stresses are significantly lower. For example, Arie & Rouse (1956) measured the maximum Reynolds shear stress to be only about 2% of $U^2_\infty$. In contrast, with the presence of vortex shedding the non-dimensional Reynolds shear stress can be observed to reach a much higher magnitude. Figure 2(*a*) shows a peak magnitude of about 13%. Similarly, experimental results at higher Reynolds number flows around circular and square cylinders also show non-dimensional Reynolds shear stress to reach as high as approximately 13% (Cantwell & Coles 1983) and 17% (Lyn *et al.* 1995), respectively.

The corresponding non-dimensional Reynolds normal stresses are shown in figures 2(*b*) (streamwise normal stress: $\overline{u'^2}$) and 2(*c*) (cross-stream normal stress: $\overline{v'^2}$). It is evident that the normalized magnitudes of the normal stresses are significantly larger than that of the shear stress, with peak values reaching 0.22 and 0.49 for the streamwise and transverse components, respectively. This behaviour remains the same at higher Reynolds numbers, as shown by Cantwell & Coles (1983) for a circular cylinder at $Re = 140000$, where the peak values of streamwise and transverse normal stresses are 0.26 and 0.44 respectively. The corresponding peak values for a square cylinder at $Re = 21400$ are even higher with $\overline{u'^2}$ and $\overline{v'^2}$ reaching 0.42 and 0.79 (Lyn *et al.* 1995). Further it is observed from figures 2(*a*)–2(*c*) that while the shear stress is antisymmetric, the normal stresses are symmetric about the wake centreline. The Reynolds streamwise normal stress reaches a local minimum, whereas the Reynolds cross-stream normal stress reaches a local maximum along the wake centreline. It can be seen that the normal stresses, in particular the streamwise component which appears in the force balance, are significant along the boundary of the mean recirculation region.

In figure 2(*d*) the distribution of pressure coefficient, $C_p$, is plotted. As observed in many early works, the pressure coefficient reaches a minimum not at the cylinder base, but at a short distance downstream. In the present case, this point of pressure minimum falls slightly upstream of the reattachment point. The pressure recovery to the free-stream value is not achieved at reattachment and in fact the reattachment pressure is lower than the base pressure. Thus it is not only that the shear stress distribution along the separating streamlines is too small to balance the pressure force, in fact, as will be seen below, the net pressure force acts in the same direction as that due to the shear stress. Clearly these two forces cannot be in balance and therefore they must be balanced by the streamwise normal stress. This result is in stark contrast to the corresponding scenario in wake flows without shear layer interactions, where the pressure and shear-stress forces oppose each other and are in near balance.

Next we will consider in figure 3(*a*) the distribution of $C_p$, $C_n$ and $C_\tau$ around the periphery of the wake bubble. $C_p$ and $C_n$ are plotted against the $y$-location of the periphery while $C_\tau$ is plotted against the $x$-location of the periphery. Owing to the symmetry of the mean wake about the wake centreline ($y = 0$), these coefficients will only be presented over the upper half of the wake. Since the origin is at the base of the bluff body, the plots of $C_p$ and $C_n$ extend over $0 < y \lesssim 0.5$ and the plot of $C_\tau$ extends over $-0.32 \lesssim x \lesssim 0.89$. As the boundary of the mean recirculation region is traced from the base (marked B in figure 1) to the separation point (marked S in figure 1) along the leeward side of the body, then to the reattachment point (marked R in figure 1) along the separating streamline, and then back to the base (marked B in figure 1) along the wake centreline, the plots of $C_p$, $C_n$ and $C_\tau$ result in a closed curve. From the

| Cross-section | $[C_p]$ | $[C_n]$ | $[C_\tau]$ | $[\tilde{C}_n]$ | $[\tilde{C}_\tau]$ | $[\hat{C}_n]$ | $[\hat{C}_\tau]$ |
|---|---|---|---|---|---|---|---|
| Circular cylinder<br>$Re = 300$ | $-0.041$ | 0.068 | 0.010 | — | — | — | — |
| Circular cylinder<br>$Re = 525$ | $-0.057$ | 0.083 | 0.014 | — | — | — | — |
| Elliptic cylinder<br>$Re = 525$ | $-0.031$ | 0.045 | 0.004 | — | — | — | — |
| Circular cylinder<br>$Re = 3000$† | $\approx -0.026$ | 0.110 | 0.084 | — | — | — | — |
| Circular cylinder<br>$Re = 3900$ | $-0.019$ | 0.098 | 0.071 | 0.046 | 0.027 | 0.052 | 0.044 |
| Circular cylinder<br>$Re = 140000$†† | $\approx -0.045$ | 0.087 | 0.043 | 0.017 | 0.006 | 0.070 | 0.037 |
| Square cylinder<br>$Re = 21400$‡ | $\approx -0.06$ | 0.130 | 0.070 | 0.050 | 0.023 | 0.080 | 0.047 |
| Normal plate<br>$Re = 250$ | 0.085 | 0.109 | 0.157 | 0.020 | 0.049 | 0.089 | 0.108 |
| Normal plate<br>$Re = 1000$ | 0.061 | 0.115 | 0.165 | — | — | — | — |
| Normal plate<br>$Re = 28000$§ | $\approx 0.032$ | 0.116 | 0.139 | 0.012 | 0.025 | 0.104 | 0.114 |

TABLE 3. Net contribution to streamwise force balance from pressure and Reynolds shear and streamwise normal stresses. Also presented are the coherent and incoherent parts of the Reynolds stresses contributions. † A. Krothapalli, personal communication (1996), †† Cantwell & Coles (1983), ‡ Lyn *et al.* (1995) and § Leder (1991).

definition of the integrals in equation (3), the area enclosed by the closed curves graphically provides the respective integrated force. Along each of these three closed loops the corresponding separation and reattachment points are marked as S and R with an appropriate subscript, $p$, $n$ or $\tau$. In following these closed loops it helps to note that all three quantities, from their definition, are identically zero at the cylinder base (B). The stress coefficients, $C_n$ and $C_\tau$ are zero along the base of the body (between B and $\mathrm{S}_n$ in the case of $C_n$ and between B and $\mathrm{S}_\tau$ in the case of $C_\tau$). Along the separated streamlines (between S and R) all three quantities are in general non-zero. Finally, by symmetry the shear-stress coefficient, $C_\tau$, is zero along the wake centreline (between $\mathrm{R}_\tau$ and B).

The streamwise force balance represented in equation (3) is equally valid for wakes where vortex interaction is prevented by a splitter plate. For this case, Roshko (1993*a*, *b*) simplified the force balance to

$$kC_{pr}H = \langle C_\tau \rangle L \tag{5}$$

where $\langle C_\tau \rangle$ is the average shear-stress coefficient along the separating streamline, $C_{pr}$ is the pressure coefficient at the reattachment point and $k$ is a constant arising from the integration of pressure coefficient. $H$ and $L$ are the half-height of the mean wake bubble and its length from the point of separation to the point of reattachment along the wake centreline (see figure 1). With values of $\langle C_\tau \rangle = 0.025$ obtained from a canonical free shear layer, $C_{pr} = 0.32$ as obtained from the Chapman–Korst theory and $k = 0.65$ determined from the data of Arie & Rouse (1956), Roshko (1993*a*, *b*) obtained a universal aspect ratio of $L/2H \approx 4.2$, in the limit of no shear layer interaction. Since the pressure recovery is not complete by the reattachment point, a revised estimate of the aspect ratio can be obtained from experimental measurements of the reattachment pressure recovery coefficient. Based on the experimental measurements of Roshko &

Lau (1965), the pressure coefficient at reattachment can be better approximated as $C_{pr} \approx 0.27$, which results in an aspect ratio of $L/2H \approx 3.5$. This simple estimate compares well with the experimentally observed aspect ratio of 3.1. Two key assumptions for the above simplified force balance are that the pressure on the leeward side of the bluff body between the two separation points is nearly a constant equal to $p_b$ and that the contribution to the force balance from the normal stress is negligible.

Figure 3(*a*) will now be examined in the light of the above discussion. It can be seen that the pressure on the leeward side ($BS_p$) shows a small but definite variation. However, since the pressure first increases away from the base and then decreases rapidly as the separation point is approached, the assumption of constant base pressure on the leeward side is reasonable and does not lead to serious error in the estimation of pressure force. In fact, this assumption becomes better at higher Reynolds numbers. However, since the reattachment pressure is lower than the base pressure, the pressure integral in equation (3) is negative indicating that the net pressure force is along the positive $x$-direction (Note that the terms on the left-hand side of equation (3) represent forces due to pressure and normal stress pointing along the negative $x$-direction.) The Reynolds shear stress is nealry zero, except near the reattachment point where it makes a small contribution. The net contribution from the shear stress is the smallest of the three. Contribution from the Reynolds normal stress is significant and it nearly balances the pressure force.

For convenient interpretation of these stress and pressure coefficient distributions it should be borne in mind that a clockwise loop (where the loop is from B to S to R and back to B) for the shear stress corresponds to a positive $[C_\tau]$ with a net force due to shear stress along the flow (or positive $x$) direction. A counterclockwise shear-stress loop corresponds to a negative $[C_\tau]$. On the other hand, based on their definition, an anticlockwise loop for $C_p$ and $C_n$ corresponds to positive $[C_p]$ and $[C_n]$ resulting in corresponding net pressure and normal stress forces acting opposite to the flow direction (or along the negative $x$-direction). Net contributions of the pressure and stress terms are presented in table 3. In the absence of viscous forces we expect $[C_p]+[C_n]$ to balance $[C_\tau]$ exactly. At this modest Reynolds number of $Re = 300$ the forces due to pressure and Reynolds stresses do not perfectly cancel each other. The difference is small and can be attributed to the viscous stresses.

### 3.2. *Other bluff bodies of cylindrical cross-section*

In the following we will examine the generality of the above results for changes in Reynolds number and the geometry of bluff body. Figure 3(*b*) shows the $C_p$, $C_n$ and $C_\tau$ distributions around the mean recirculation region of a circular cylinder at a Reynolds number of 525. The corresponding non-dimensional length and half-height are computed as 1.19 and 0.52, respectively. It is therefore somewhat shorter and thicker than the mean wake at $Re = 300$. The pressure and stress coefficients appear very similar to the lower Reynolds number case shown in figure 3(*a*). The pressure recovery remains far from complete by the reattachment point and the pressure here is lower than the base pressure. The shear stress still makes only a small contribution and the primary force balance is between the pressure force which is pointed along the positive $x$-direction and the Reynolds streamwise normal stress pointed along the negative $x$-direction. Owing to the higher Reynolds number, the relative contribution from the viscous stresses, given by $[C_p]+[C_n]-[C_\tau]$, has somewhat decreased.

Figure 3(*c*) shows the $C_p$, $C_n$ and $C_\tau$ distributions around the mean recirculation region of an elliptic cylinder at zero angle of attack and with a major-to-minor axis ratio of 2 at a Reynolds number of 525 (Mittal & Balachandar 1995*a*). The flow is aligned with the major axis of the elliptic cross-section of the cylinder and therefore the minor axis is considered as the effective diameter, $D$, of the cylinder and used as the reference length scale. The non-dimensional length ($L/D$) and half-height ($H/D$) of the corresponding wake are about 1.98 and 0.5, respectively. Here $D$ is the projected width of the cylinder as seen by the flow, which is equal to the minor axis of the elliptic cylinder. Since the bluffness of the cylinder has decreased, the aspect ratio of the wake bubble has increased, resulting in a thinner and longer recirculation region. The pressure and stress coefficients qualitatively appear similar to the circular cylinder cases discussed above, but are smaller in magnitude. For example, the peak values of normalized Reynolds streamwise normal, transverse normal and shear stresses for the elliptic cylinder are respectively, 0.13, 0.31 and 0.09 (Mittal & Balachandar 1995*a*). The corresponding peak values for the circular cylinder at $Re = 525$ are respectively 0.26, 0.62 and 0.15 (Mittal & Balachandar 1995*a*). Thus the Reynolds stresses are significantly smaller for the elliptic cylinder at zero angle of attack. However the shear layer velocity, $U_e$, is lower for the elliptic cylinder and somewhat compensates for the lower Reynolds stresses in the evaluation of the stress coefficients (see (2)). The shear layer velocity, $U_e$, used in the various cases is listed in table 2. In figure 3(*c*) it is interesting to note that the shear stress changes sign along the separating streamline. Close to the cylinder, over the first quarter of the separating shear layer ($-0.5 \leqslant x \leqslant 0$), the shear stress is nearly zero. Over $0 \leqslant x \leqslant 1.1$, the shear-stress coefficient along the top side of the wake ($y > 0$) is negative and only near the reattachment point does the shear-stress coefficient become positive. The resulting net contribution to the streamwise force from the Reynolds shear stress, $[C_\tau]$, is observed to be very small, as seen in table 3.

Next in figure 3(*d*) we show $C_p$, $C_n$ and $C_\tau$ for a circular cylinder at $Re = 3900$ (Mittal 1996). At this Reynolds number the instability has moved upstream into the shear layers and manifests itself as Bloor–Gerrard vortices (Bloor 1964; Gerrard 1978). A number of points require attention. With this increase in Reynolds number, the non-dimensional length and half-width of the wake have increased to 1.99 and 0.6, and the aspect ratio is slightly larger than its value at the lower Reynolds numbers. The shear-stress coefficient reaches its peak value of about 0.1 near the reattachment point, which represents a slight increase over the lower Reynolds number cases of 0.08. More importantly, at this higher Reynolds number the shear stress remains significant over much of the separating shear layer, except at its upstream end, close to the body. Thus the Reynolds shear stress now makes an appreciable contribution to the overall force balance. The streamwise normal stress around the mean wake bubble periphery is still large, but the pressure coefficient has decreased in magnitude. The pressure along the separating streamline ($\mathrm{S_p R_p}$) near the reattachment point is now nearly a constant and is lower than the pressure on the leeward side of the body. Therefore the net streamwise force due to pressure, $[C_p]$, although relatively small, is still negative and points along the positive $x$-direction. At this higher Reynolds number the viscous stresses are observed to be negligible and the primary balance is between the Reynolds stresses and pressure.

Also plotted in figure 3(*d*) are the results of stress coefficients obtained from the PIV measurements of A. Krothapalli (1996, personal communication) at $Re = 3000$. The distributions of experimentally measured stress coefficients and their computational counterpart show a similar trend. Based on an approximate balance between the pressure force and Reynolds stresses, $[C_p]$ for the experiment can be estimated to be $-0.026$. Furthermore, the computational and experimental results are in good agreement. For example, the experimentally measured length and half-width of the

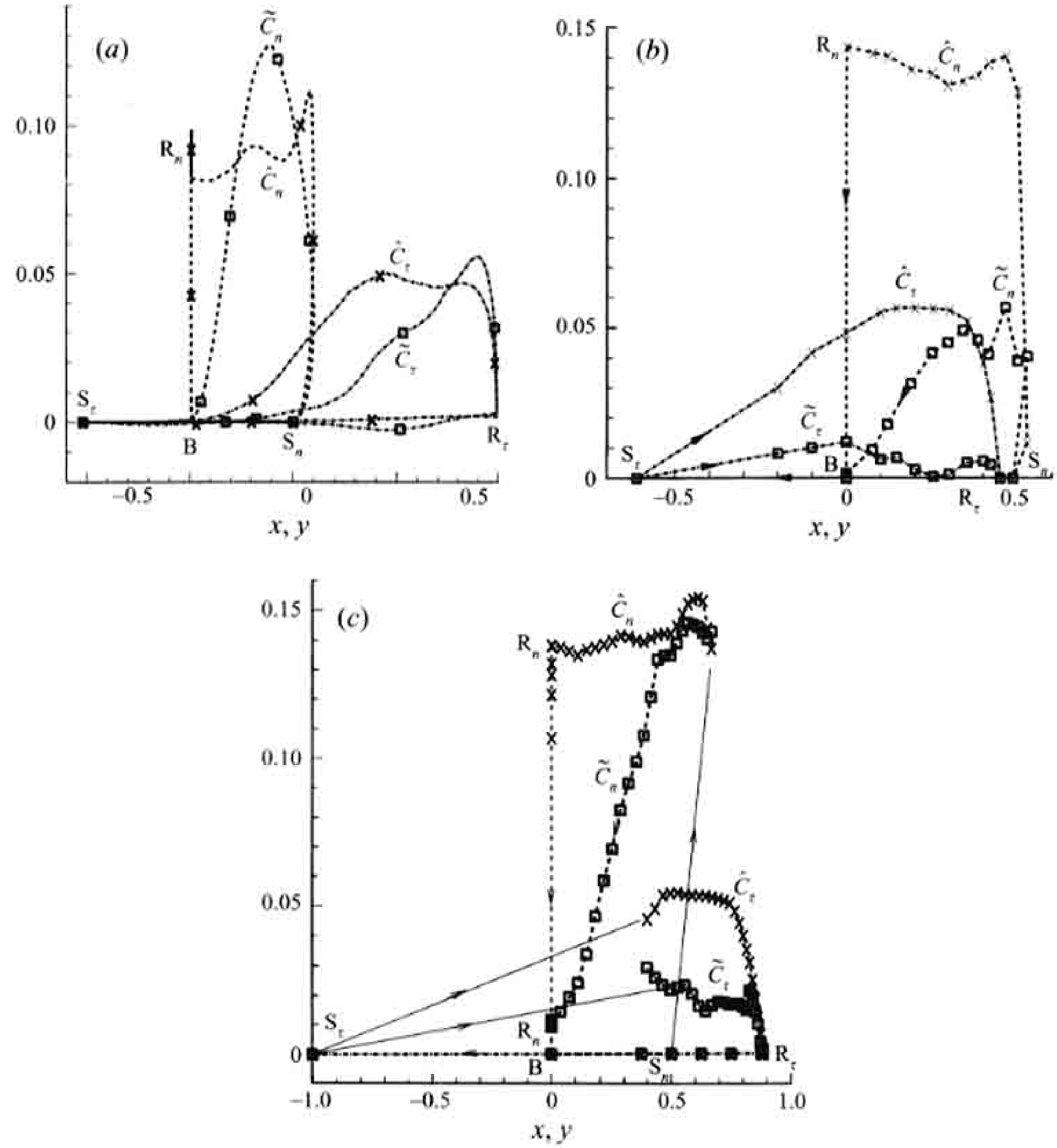

FIGURE 4. Variation of computed coherent and incoherent componets of the shear and streamwise normal stress coefficients along the boundary of the mean separation bubble. Dashed line corresponds to the normal-stress coefficient and the dash–dot line corresponds to the shear stress coefficient; □, coherent contribution and ×, incoherent contribution. (*a*) Circular cylinder at $Re = 3900$ (Mittal 1996). (*b*) The experimental results of Cantwell & Coles (1983) for a circular cylinder at $Re = 140000$. (*c*) The experimental results of Lyn *et al.* (1995) for a square cylinder at $Re = 21400$.

wake are $1.8D$ and $0.64D$. The computed peak normalized stresses in the wake region are 0.21, 0.43 and 0.12 for $\overline{u'^2}$, $\overline{v'^2}$ and $\overline{u'v'}$, respectively and the corresponding values from the experiments are 0.30, 0.48 and 0.15.

In figure 3(*e*) the distributions of stress coefficients evaluated from the flying-hot-wire measurements of Cantwell & Coles (1983) for flow over a circular cylinder at $Re = 140000$ are plotted. At this Reynolds number the attached boundary layer still remains laminar at the separation point, but the transition point in the shear layer has moved up closer to the separation point. The mean recirculation region has significantly shrunk in size with the length being only $1.1D$. The peak values of $\overline{u'^2}$, $\overline{v'^2}$ and $\overline{u'v'}$ are still close to their lower Reynolds number values at approximately 0.26, 0.44 and 0.13, respectively. The pressure coefficient along the base of the cylinder is also plotted. The variation in the pressure coefficient along the cylinder base seems to be somewhat larger at this higher Reynolds number than in the previous cases. A simple balance of forces suggests that the average pressure coefficient along the separating streamlines is approximately $-0.05$. In other words, the average pressure along the leeward side of the cylinder is still higher than the average pressure along the separating streamlines. Therefore like the lower Reynolds number cases, the net pressure force is directed along the positive $x$-direction. Since the pressure coefficient is not measured all around the mean wake, in table 3 $[C_p]$ is estimated through an approximate force balance: $[C_p] \approx [C_\tau] - [C_n]$.

Next we examine the experimental results of Lyn *et al.* (1995) for flow over a square cylinder at $Re = 21400$. The flow over a square cylinder fundamentally differs from flow over circular and elliptic cylinders in that the separation points are held fixed at the front two sharp edges of the square cylinder. As a result the separating layers are thinner for a square cylinder. Furthermore, while in the case of a circular cylinder the base of the cylinder extends about half a diameter from the separation point in the streamwise direction, in a square cylinder the base extends nearly twice as far into the wake. In this sense the square cylinder is closer to the elliptic cylinder of aspect ratio 2. The mean flow measurements of Lyn *et al.* (1995) along the centreline of the wake gives a wake length of $1.88D$, but the half-height of the wake can only be approximately estimated as $0.74D$. Figure 3($f$) shows a plot of $C_n$ and $C_\tau$ around the wake bubble. The experimental data extend only part way up the separating streamline and the stress coefficients over the reminder of the separating streamline, close to the separation point near the front top leading edge, is simply sketched as a thin solid line, in order to complete the closed loops. In spite of the significant differences in the geometry of the bluff body, the distribution of stress coefficients around the wake bubble is both qualitatively and quantitatively similar to the corresponding distributions in the higher Reynolds number circular cylinder cases. However the measured values of the peak normal and shear stresses, $\overline{u'^2} = 0.42$, $\overline{v'^2} = 0.79$ and $\overline{u'v'} = 0.17$ are somewhat higher than those of the circular cylinder. These higher levels of Reynolds stress are comparable to those measured by Durao, Heitor & Perira (1986, 1988) in the wake of a square cylinder at $Re = 14000$. The shear stress is likely to remain significant over most of the shear layer and make a significant contribution to the force balance. The Reynolds streamwise normal stress around the wake is larger than the shear stress suggesting that the net pressure force is still directed along the positive $x$-direction.

### 3.3. *Coherent and incoherent contribution to Reynolds stress*

The change in behaviour from the low-Reynolds-number cases ($Re \leqslant 525$) to the higher-Reynolds-number cases ($Re \geqslant 3000$) is not entirely surprising, given the importance of transition location relative to the separation and reattachment points (Chapman *et al.* 1957; Roshko & Fiszdon 1969). At the lower Reynolds numbers the Reynolds stress in the near wake is predominantly due to the time-dependent nature of the Kármán vortex street. At higher Reynolds numbers, although the velocity and pressure fields are chaotic in the new wake, a dominant frequency corresponding to a large-scale Kármán vortex shedding phenomenon can still be observed. However, since transition occurs along the separated shear layers, apart from the dynamics of the rolled-up vortex street, the instability of the separating shear layers and the near-wake turbulence also contribute to the Reynolds stress.

In order to better understand the different contributions in the low- and high-

Reynolds-number regimes, we applied the phase-averaging procedure suggested by Reynolds & Hussain (1972) and Cantwell & Coles (1983). The flow variables $(\boldsymbol{u}, p)$ are considered to be made up of three components: a long-time- and span-averaged mean $(\bar{\boldsymbol{u}}, \bar{p})$, a periodic mean component $(\tilde{\boldsymbol{u}}, \tilde{p})$ and a random component $(\hat{\boldsymbol{u}}, \hat{p})$:

$$(\boldsymbol{u}, p) = (\bar{\boldsymbol{u}}, \bar{p}) + (\tilde{\boldsymbol{u}}, \tilde{p}) + (\hat{\boldsymbol{u}}, \hat{p}). \tag{6}$$

From the above, a coherent component can be defined as the sum of the time-averaged and the periodic mean parts as $(\bar{\boldsymbol{u}}, \bar{p}) + (\tilde{\boldsymbol{u}}, \tilde{p})$. The coherent component is computed from a long-time average of the flow field at constant phase, where in experiments the phase is determined from a reference signal, either for pressure or velocity, at a single point (Cantwell & Coles 1983; Perry & Steiner 1987; Lyn *et al.* 1995). The coherent component is therefore also referred to as the phase-averaged component. An average of the coherent component over all the different phases will erase the phase information and result in the time-averaged mean. Since in the present study we will be concerned with the coherent component only in the near-wake region, contamination by phase jitter (Hayakawa & Jussain 1989) may not be of great concern. In computing the phase average the primary interest is in resolving only the dominant frequency of the Kármán vortices and therefore typically only a limited number of phases (of the order of 16) are used. Thus the random component, which constitutes the incoherent part, accounts for all other fluctuations. It is important to note that the random component is not limited to small-scale turbulent fluctuations alone. At low Reynolds numbers, the complex dynamics of the laminar shear layers and the rolled-up Kármán vortices, such as the low-frequency oscillation, if present, appears as part of the incoherent random component. Furthermore, large-scale three-dimensionality, which is present at Reynolds numbers even as low as 190 (Williamson 1996), can contribute to the incoherent component.

The periodic mean $(\tilde{\boldsymbol{u}}, \tilde{p})$ and random components $(\hat{\boldsymbol{u}}, \hat{p})$ together account for all the fluctuations, $(\boldsymbol{u}', p')$, about the long-time average. The conventional Reynolds stress components, $\overline{u'^2}, \overline{v'^2}$, and $\overline{u'v'}$ presented in figures 2 and 3 are based on this total fluctuation. The Reynolds stress can then be split into a coherent and an incoherent component. The coherent component is defined as $\overline{\tilde{u}^2} = \sum (\tilde{u})^2$ and $\overline{\tilde{u}\tilde{v}} = \sum \tilde{u}\tilde{v}$, where summation is over all the phases that make up a shedding cycle. The incoherent component is then defined as $\overline{\hat{u}^2} = \overline{u'^2} - \overline{\tilde{u}^2}$ and $\overline{\hat{u}\hat{v}} = \overline{u'v'} - \overline{\tilde{u}\tilde{v}}$ (Reynolds & Hussain 1972). The corresponding stress coefficients can also be written as $(\tilde{C}_n, \tilde{C}_\tau)$ and $(\hat{C}_n, \hat{C}_\tau)$. Wherever appropriate, table 3 also provides the net contribution to the force balance from the coherent and incoherent components of streamwise normal and shear stresses.

Figures 4(*a*), 4(*b*) and 4(*c*) plot the coherent and incoherent Reynolds stress coefficients for the three high-Reynolds-number cases: circular cylinder at $Re = 3900$ and 140000 and square cylinder at 21400, respectively. The computation of phase average and the separation of Reynolds stresses into coherent and incoherent parts from the experimental measurements have been presented in Cantwell & Coles (1983) for the circular cylinder at $Re = 140000$ and in Lyn *et al.* (1995) for the square cylinder. In the $Re = 3900$ circular cylinder case, the shedding cycle is divided into 12 phases of equal extent, with the beginning of each cycle marked by the peak in the global lift coefficient. It can be seen from the $Re = 140000$ case that along the periphery of the mean recirculation region the coherent contribution to the shear stress is nearly zero and that the large value of shear stress measured along the separating streamline is mostly due to the incoherent part arising from the shear layer instability. At $Re = 3900$, the coherent part of shear stress, $\tilde{C}_\tau$, makes an appreciable contribution to the force balance and it resembles the shear stress distribution at $Re = 525$ seen in figure 3(*b*). The incoherent contribution to the shear stress is larger than the coherent contribution. Results for the intermediate $Re = 21400$ case are somewhere in between with the coherent component of shear stress not entirely negligible, but significantly smaller than the incoherent component. The peak value of the incoherent contribution to shear stress is consistently around 0.05 for all the three cases, but a comparison of the $Re = 3900$ and 140000 cases shows that as the transition point moves upstream with increasing Reynolds number, the incoherent contribution to the shear stress increasingly becomes non-zero along the shear layer close to the separation point. Thus with increasing Reynolds number the overall contribution from the incoherent component of the shear stress can be observed to increase.

At $Re = 3900$ the coherent component of the streamwise normal stress is comparable to the incoherent component. As the Reynolds number increases, since the shear layers are increasingly turbulent, the contribution from the coherent part significantly decreases and the incoherent component arising from the turbulent fluctuations plays the dominant role. While at $Re = 3900$ the peak value of the coherent component of normal stress is larger than the peak value of the incoherent component, at $Re = 140000$ the peak value of the incoherent component is significantly higher than the coherent component. The crossover seems to occur around $Re \approx 20000$.

From the above results for bluff bodies of cylindrical cross-section it seems reasonable to conclude that the contribution from the coherent component of the Reynolds shear stress to the force balance is in general small. Furthermore at higher Reynolds numbers, when the transition point has moved well up into the shear layers, the coherent contribution to streamwise normal stress plays only a minor role in the force balance. In other words, at high Reynolds numbers the coherent part of Reynolds stress arising from the periodic evolution of the Kármán vortices may not be very important. On the other hand, the incoherent component, which can largely be ignored at the lower Reynolds numbers, plays an increasingly important role at higher Reynolds numbers. It must be stressed that the above statements pertain only to the distribution along the boundary of the mean wake recirculation region. For example, the coherent part of the shear stress, $\tilde{C}_r$, can still be significant inside and outside the mean recirculation region.

### 3.4. *Results for a normal plate*

We now investigate flow around a normal flat plate without a splitter plate and consider the force balance of its wake. It will be seen below that the results obtained for this case of a normal plate are significantly different from those of the cylindrical bluff bodies discussed in the previous sections. The separation points on a normal plate are fixed at the edges. Furthermore the angle the separating streamline makes with the horizontal as it leaves the surface is much larger in a normal plate, resulting in a much longer and thicker wake bubble than that of a circular cylinder. These features of the normal plate are also shared by the square cylinder. In fact, the square cylinder can be considered as a normal plate with an afterbody. As will be seen below the presence of the afterbody significantly alters the dynamics of the shear layers as well as the Reynolds stress and pressure distributions.

In order to highlight this difference we first consider direct numerical simulation results of flow over a zero-thickness normal flat plate at $Re = 250$. In brief the governing time-dependent Navier–Stokes and continuity equations were solved in three dimensions using a higher-order finite difference scheme. A fifth-order upwind-biased scheme is used for the convective term, while a fourth-order central difference

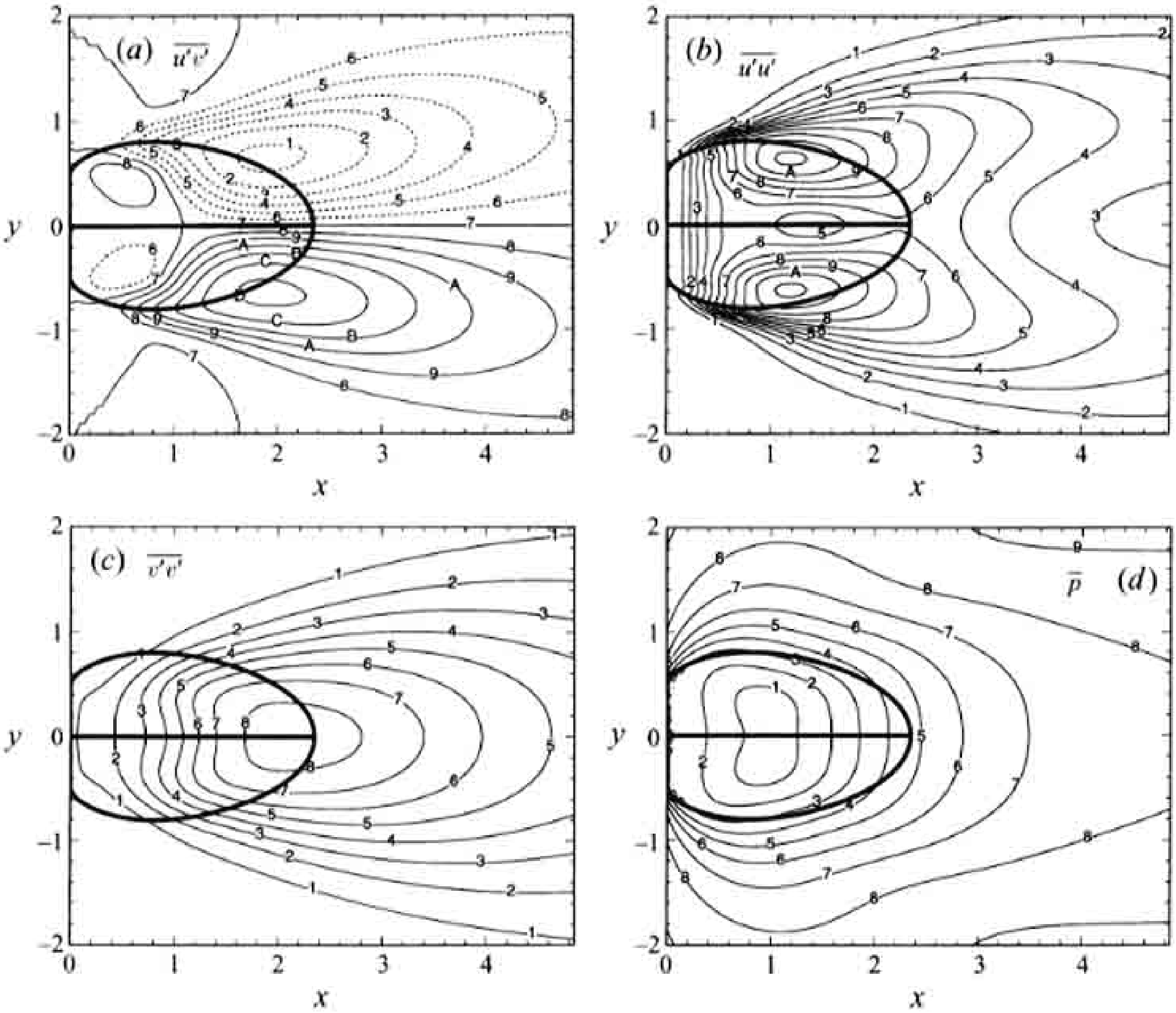

FIGURE 5. Reynolds stress and pressure distribution in the wake of a normal plate at a Reynolds number of 250. Solid and dashed lines denote positive and negative values respectively. The mean separation streamline is shown by a thick line. (*a*) Reynolds shear stress: 13 contours marked 1 to D corresponding to values −0.12 to 0.12 in steps of 0.02. (*b*) Reynolds streamwise normal stress: 11 contours marked 1 to B corresponding to values 0.02 to 0.22 in steps of 0.02. (*c*) Reynolds cross-stream normal stress: 8 contours marked 1 to 8 corresponding to values 0.05 to 0.4 in steps of 0.05. (*d*) Mean pressure coefficient: 9 contours marked 1 to 9 corresponding to values −0.2 to 0.6 in steps of 0.1.

scheme is used for the diffusion term and the Pressure Poisson equation. Discretization in time uses a second-order-accurate time-splitting procedure with a fully explicit Adams–Bashforth scheme for both the convective and diffusive terms. The computational domain extends 5 non-dimensional units upstream of the normal plate to 20 non-dimensional units in the downstream direction. In the cross-stream direction the computational domain extends from −8 to +8 non-dimensional units. The spanwise width of the computational domain is chosen to be $2\pi$ and periodic boundary conditions are applied along the spanwise direction. Uniform free-stream conditions are applied at the inlet and at the top and bottom boundaries of the computational domain. A convective boundary condition is applied at the outlet. A grid of $192 \times 128 \times 48$ along the streamwise, transverse and spanwise directions is employed with a non-uniform mesh along $x$ and $y$. Simulations were carried out for a long duration of 512 non-dimensional time units covering approximately 72 shedding cycles. Numerical details can be found in Najjar (1994).

In figures 5(*a*), 5(*b*), 5(*c*) and 5(*d*) we present the distributions of normalized

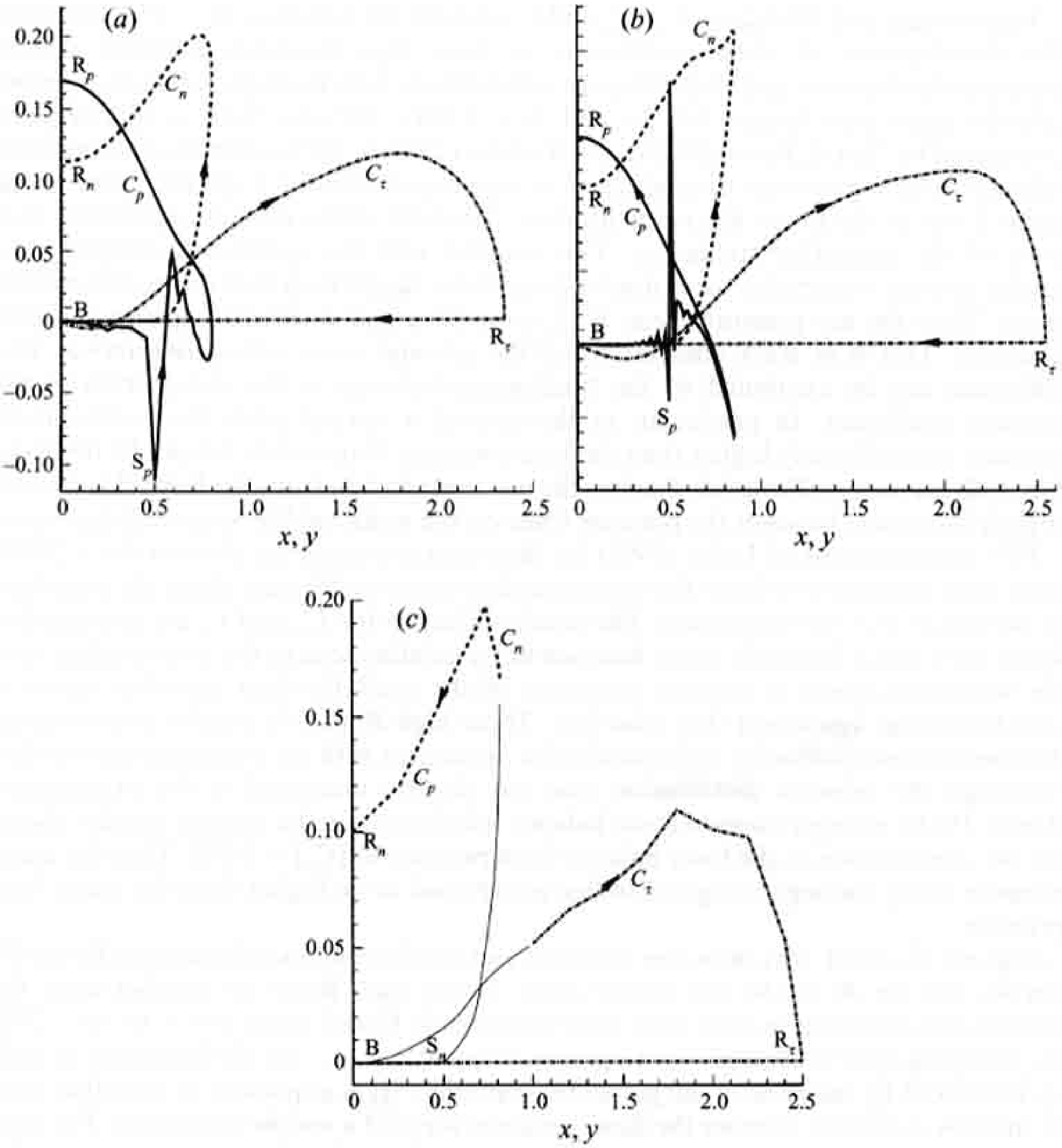

FIGURE 6. Same as figure 3(*a*) for a normal plate at (*a*) $Re = 250$, (*b*) $Re = 1000$ (Najjar & Vanka 1995), (*c*) the experimental measurements of Leder (1991) at $Re = 28000$.

Reynolds shear and streamwise normal stresses along with the distribution of the pressure coefficient in the near-wake region of a normal plate at $Re = 250$. For visual reference, the outline of the mean recirculation region has been superimposed in these figures. The Reynolds stresses appear qualitatively similar to the corresponding distributions for a $Re = 300$ circular cylinder shown in figures 2(*a*) and 2(*b*), but some differences can also be observed. The magnitude of normal stresses is larger than that of the shear stress. The peak values of $\overline{u'^2}, \overline{v'^2}$ and $\overline{u'v'}$ are respectively 0.23, 0.42 and 0.13. These peak values of Reynolds stress components compare well with those of the circular cylinder. However, both the normalized length ($L/D = 2.35$) and half-height ($H/D = 0.8$) are significantly larger for the normal plate than for the circular cylinder. Since the increase in length has somewhat outweighed the increase in width, the aspect ratio ($L/H$) is also large for the normal plate. Correspondingly the stress and pressure distributions have extended further along the downstream direction.

Figures 6(*a*) and 6(*b*) show $C_p$, $C_n$ and $C_\tau$ around the wake for $Re = 250$ and 1000. The distributions of stress coefficients at these two Reynolds numbers remain qualitatively the same and they compare satisfactorily with the high-Reynolds-number cylinder cases (see figures 3*d*, 3*e* and 3*f*). Unlike the case with a splitter plate considered by Arie & Rouse (1956) and Roshko (1993*a*), the contribution to the force balance from streamwise normal stress is significant without a splitter plate in the wake. Even at the lower Reynolds number, the shear stress remains significant over most of the separating streamline. This coupled with the significantly longer wake results in a net streamwise force due to shear stress larger than that due to the normal stress. Thus the net pressure force, $[C_p]$, is positive and is directed against the flow direction. This is in stark contrast to all the cylinder cases considered above. This difference can be attributed to the fundamental change in the distribution of the pressure coefficient. In particular, in the case of a normal plate the reattachment pressure is significantly higher than the base pressure. From table 3 it can be observed that with increase in Reynolds number the net contribution from the Reynolds stresses slightly increases; however the pressure force on the wake bubble somewhat decreases.

PIV measurements of Leder (1991) for flow over a normal flat plate at $Re = 28000$ have been digitized to obtain the corresponding stress coefficients along the periphery of the mean recirculation region. The results obtained for $C_n$ and $C_\tau$ are presented in figure 6(*c*). Since Reynolds stress data are not available close to the normal plate near the separation point, a possible extension of the available data into this region is sketched in the figure as a thin solid line. These high-Reynolds-number experimental data are in close qualitative and quantitative agreement with the computational results. Although the pressure distribution was not directly measured in the experiments (Leder 1991), an approximate force balance which ignores the viscous stresses places the net contribution to the force balance from pressure at $[C_p] = 0.032$. Thus the mean pressure along the separating streamline is expected to be higher than the mean base pressure.

Figures 7(*a*) and 7(*b*) show the coherent and incoherent contributions to Reynolds stresses for the $Re = 250$ and 28000 cases. In the high Reynolds number case, the coherent and incoherent data were obtained directly from Leder (1991). At $Re = 250$, the shedding cycle is divided into 12 phases of equal extent, with the beginning of each cycle marked by the peak in the global lift coefficient. It is important to note that even at this low Reynolds number the flow variation was not a simple sinusoidal. The time variation in the lift and drag coefficients shown in figure 8 indicates the presence of a low frequency in addition to the dominant shedding frequency. Here, owing to the idealized normal plate of zero thickness employed in the computations, the lift force is entirely due to the viscous stresses and the drag force is from pressure. It can be observed that the shedding frequency, or the time separation between adjacent lift peaks, varies considerably from shedding cycle to shedding cycle. Lisoski (1993) has shown a similar variation in lift and drag coefficients for a normal plate at $Re = 5000$ (also see Roshko 1993*a*). Therefore, in computing the phase average, the computational data dumps which were uniformly spaced in time were assigned to appropriate phase bins based on the lift coefficient. Each bin was averaged to obtain the phase-averaged flow field, which then yielded the coherent component of the Reynolds stress.

It can be observed that similarly to the circular cylinder wake the coherent contribution to Reynolds stresses decreases with Reynolds number. However, the incoherent component of both the streamwise normal and shear stresses are remarkably close at the two Reynolds numbers. The existence of the incoherent component to

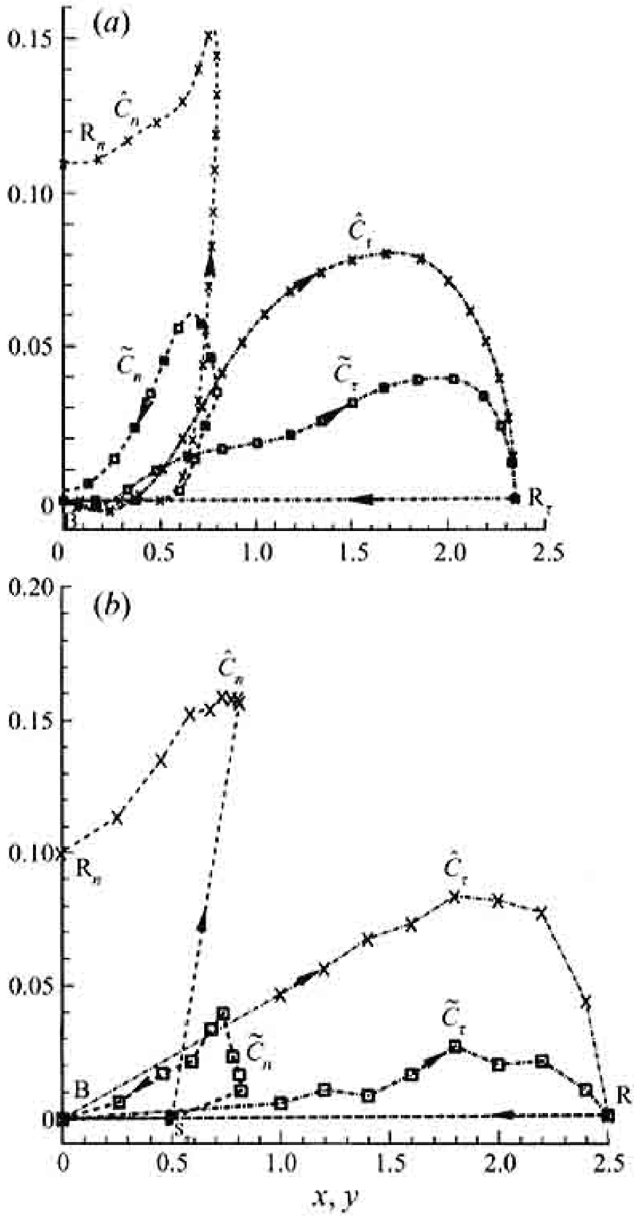

FIGURE 7. Same as figure 4(*a*) for a normal plate at (*a*) $Re = 250$, (*b*) for the experimental measurements of Leder (1991) at $Re = 28000$.

Reynolds stresses even at Reynolds numbers as low as 250 seems surprising. From its definition it is clear that the coherent part of the Reynolds stress accounts only for the fluctuation about the time mean due to an average representative shedding cycle. It is evident from figure 8 that the flow variation from cycle to cycle is strong due to the low-frequency oscillations observed in the shedding process (Lisoski 1993; Roshko 1993*a*; Lyn & Rodi 1994; Najjar 1994; Najjar & Balachandar 1997). This complex behaviour of the shedding process is the contributing factor for the incoherent component of the Reynolds stress. At higher Reynolds numbers, when the shear layers are transitional, small-scale turbulent fluctuations can also contribute to the incoherent component.

### 3.5. *Kármán vortex dynamics, mean wake recirculation region and coherent stresses*

From the above results it appears that there are a number of common features that are shared by all the geometries considered here and perhaps by all bluff bodies in general. First, it is observed that over the entire range of Reynolds number the coherent contribution to the Reynolds shear stress is sufficiently small along the separating streamlines that it can be ignored in the force balance. Secondly, in all the low-

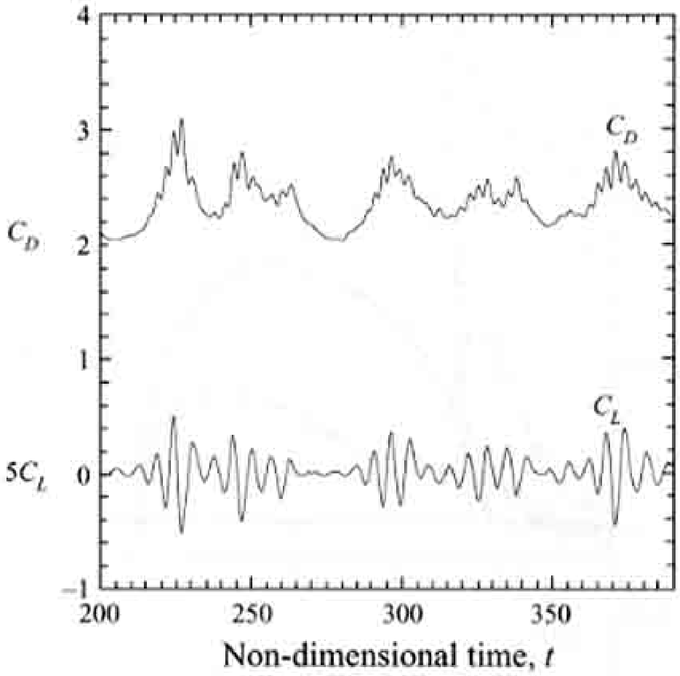

FIGURE 8. Time variation of the drag and lift coefficients for the flow over a normal plate at $Re = 250$.

Reynolds-number cases considered the contribution to the force balance from the coherent component of the Reynolds streamwise normal stress is significant. By definition, the coherent part of Reynolds stress arises from the periodic evolution of the span-averaged two-dimensional Kármán vortices. Furthermore, the shape of the mean wake remains reasonably the same for all the different bluff bodies considered, although the actual size in terms of length and width shows some variability. The shape and size of the mean recirculation region, obtained from the mean velocity field, are again largely dictated by the dynamics of the Kármán vortices. Therefore in order to explain these generic behaviours, coherent Reynolds stresses around the wake and their relation to the evolution of the Kármán vortices need to be explored.

To illustrate the vortex dynamics, as an example in figure 9 contours of span- and time-averaged spanwise vorticity, $\omega_z$, are shown at six different time instances, each separated by one-tenth of a shedding cycle for the $Re = 300$ circular cylinder case. The entire sequence covers one half of a shedding cycle. The spanwise vorticity distribution over the next half of the shedding cycle will be approximately the mirror image of the ones shown about the wake centreline. Thus the evolution of the vortices can be followed over the entire shedding cycle. In figure 9 the trajectories of both the clockwise and counterclockwise rotating vortices are traced out by the filled dot symbols. These trajectories have been determined by identifying the centroid of the spanwise vortices as they form and convect downstream (Cantwell & Coles 1983). In the early stages of the formation process, the vortex centre is not easily identifiable in terms of the spanwise vorticity distribution, but can be captured by a careful examination of the imaginary eigenvalues of the velocity gradient tensor, which has been well established to extract vortices with local circular or spiralling streamlines (Dallmann *et al.* 1991; Chong, Perry & Cantwell, 1990; Mittal & Balachandar 1995*b*). The trajectory shown in this figure gives a good representation of the motion of the spanwise vortices during their evolution and this qualitative picture will be sufficient for the present investigation. Since each adjacent symbol represents the position of the vortex after 1/10 of the shedding period, the distance between neighbouring symbols provides qualitative information on the velocity of the vortex core during the various stages of the shedding

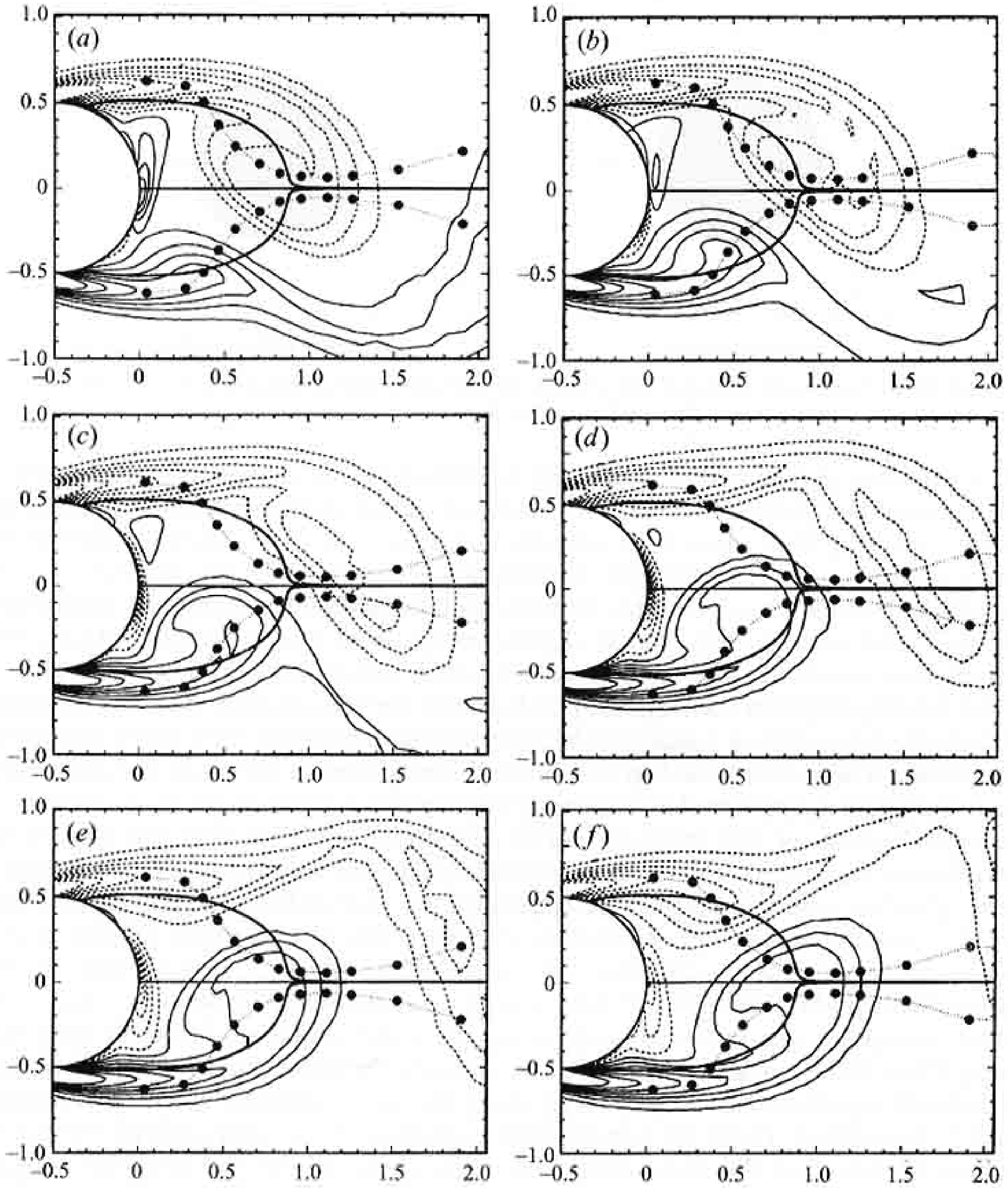

FIGURE 9. A series of plots showing contours of span-averaged spanwise vorticity in the near wake of a circular cylinder at $Re = 300$. Each plot is separated in time by 1/10 of the shedding period and the six plots cover one half of the shedding period. Solid and dashed lines denote positive and negative values respectively. The mean separation streamlines and the vortex trajectories have also been superposed.

cycle. The very first point in the immediate wake of the cylinder corresponds to the position of incipient roll-up of the spanwise vortex.

A close observation of the trajectory and the vortex shedding process shows that the movement of the spanwise vortices can be divided into three distinct phases. These phases have been marked in figure 2 where the location of the Kármán vortices has also been marked by filled dots. Phase I extends over half a shedding period beginning from the formation of a new spanwise vortex and during this stage the vortex, which is in the process of roll-up, slowly moves towards the centreline. Phase II also extends over

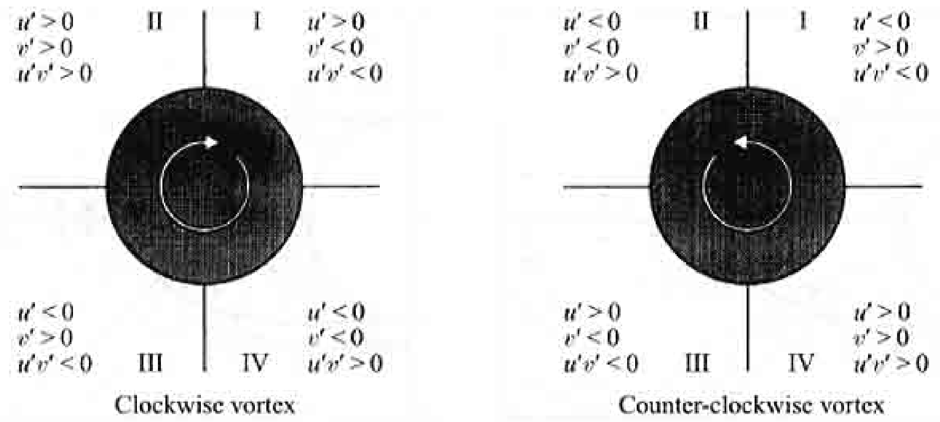

FIGURE 10. Schematic showing the velocity perturbation and correlation produced by two idealized spanwise Kármán vortices.

half a shedding period and its beginning is marked by the change in the direction of movement of the spanwise vortex. This direction change is due to the movement of the vortex from the other shear layer towards the wake centreline. During Phase II the vortex convects slowly along the streamwise direction while staying close to the centreline. During Phase III, the vortices initially accelerate along the streamwise direction and subsequently move slightly away from the centreline. Again this movement is a result of the vortex from the other shear layer entering Phase II.

The relation between the trajectory of Kármán vortices and the shape of the mean wake recirculation region is explored by superimposing on figure 9 the mean separating streamlines, which define the top and bottom boundaries of the recirculation region. From the figure it appears that the mean wake encloses most of the first and part of the second phase of the spanwise vortex evolution. We note that the size of the recirculation region can be determined primarily from the location of the reattachment point, since the separation points are approximately known from the bluff body shape and the nature of separation. While from symmetry the mean vertical velocity is zero along the entire wake centreline, the streamwise velocity changes sign at the reattachment point. The effect of both clockwise and counterclockwise vortices is to induce a negative streamwise velocity along the wake centreline. It can be seen that during Phase I the vortices primarily move towards the wake centreline and therefore the induced negative streamwise velocity along the wake centreline is strongest around $x \approx 0.5$. In contrast, Phase III is marked by a decrease in the ability of the vortices to produce backflow at the wake centreline. This is due to the fact that the vortices accelerate in the streamwise direction and also move away from the wake centreline. From these observations it stands to reason that the reattachment point will lie somewhere along the Phase II region of the trajectory. Figure 2 clearly shows that the reattachment point lies in the early part of Phase II.

Next we attempt to understand the coherent contribution to Reynolds stress distributions along the separating streamlines based on the dynamics of the clockwise and counterclockwise Kármán vortices. Insight into the Reynolds stress distribution can be obtained by considering the velocity perturbation induced by the spanwise Kármán vortices. Figure 10 is a schematic showing the velocity perturbations induced by two idealized spanwise Kármán vortices. It is clear from this figure that the streamwise velocity perturbations to the top and bottom of the clockwise vortex are positive and negative, respectively, while the vertical velocity perturbations to the left and right of the clockwise vortex are positive and negative respectively. The perturbations produced by the counterclockwise vortices are exactly opposite to those

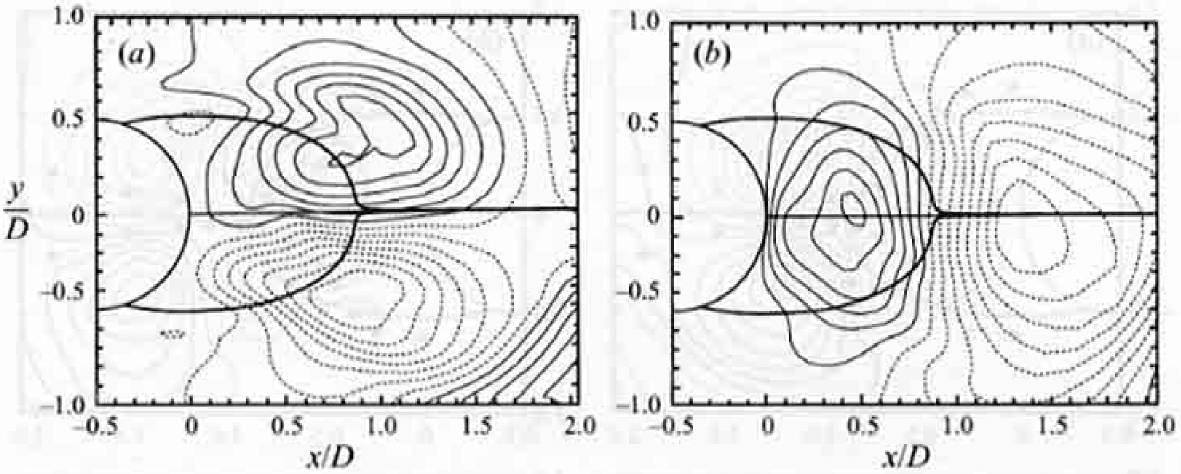

FIGURE 11. Contours of the velocity fluctuation corresponding to the Kármán vortex at the phase instance shown in figure 9(*a*). The mean separation streamlines are superposed. (*a*) Streamwise perturbation velocity, and (*b*) cross-stream ($y$) perturbation velocity.

produced by the clockwise vortex. However, both vortices produce exactly the same distribution of the $\tilde{u}\tilde{v}$ correlation. The distribution of this quantity is divided into four quadrants whose axes are marked in the figure by thin lines and the origin is centred about vortex centre. The sign of Reynolds shear stress seems to alternate as negative, positive, negative and positive from quadrant I to quadrant IV, also marked in the figure.

At $Re = 300$, the incoherent contribution to Reynolds stress is small and the total Reynolds stress is approximately given by the coherent part alone. Contours of the periodic component of the streamwise and transverse velocity fluctuations, $\tilde{u}$ and $\tilde{v}$, corresponding to the phase instances shown in figure 9 (*a*), are shown in figures 11 (*a*) and 11(*b*) respectively. It can be clearly seen that velocity perturbations are mainly dictated by the clockwise vortex situated near the wake centreline (figure 9*a*) and the distribution of the perturbations is qualitatively as indicated in figure 10. The distribution of Reynolds stress is consistent with the perturbation velocity distribution shown in figure 11.

Figure 12 shows the instantaneous non-dimensional $\tilde{u}\tilde{v}$ distribution at the six time instances shown in figure 9. Figure 12(*a*) clearly shows the four quadrants of the distribution and this can be easily correlated with the $\tilde{u}$- and $\tilde{v}$-distributions shown in figure 11. The four-quadrant type distribution is also observed in figure 12(*b*, *e*, *f*) and this indicates that the Reynolds stress distribution is mainly due to one strong spanwise vortex. In contrast, the $\tilde{u}\tilde{v}$-distribution is slightly more complex in figure 12(*c*, *d*) and this is due to the fact that at these phases both vortices are strong enough to influence the $\tilde{u}\tilde{v}$-distribution.

The superposition of the vortex trajectory on the Reynolds shear stress indicates that the coherent part of the Reynolds shear-stress distribution in the near wake appears to be mainly dictated by the vortex which is in Phase II. The vortex which has entered Phase III is sufficiently downstream that its influence in and around the wake bubble is small. The vortex which is in its incipient stages of formation in Phase I is also too weak to make a strong contribution. However, in Phase II, the mature vortices approach closest to the wake centreline and the shear-stress contributions of the clockwise and counterclockwise vortices reinforce each other. Thus the vortices in Phase II represent the coherent Reynolds-shear-stress producing 'event' of the shedding cycle. In fact the overall shear-stress distribution shown in figure 2(*a*) looks

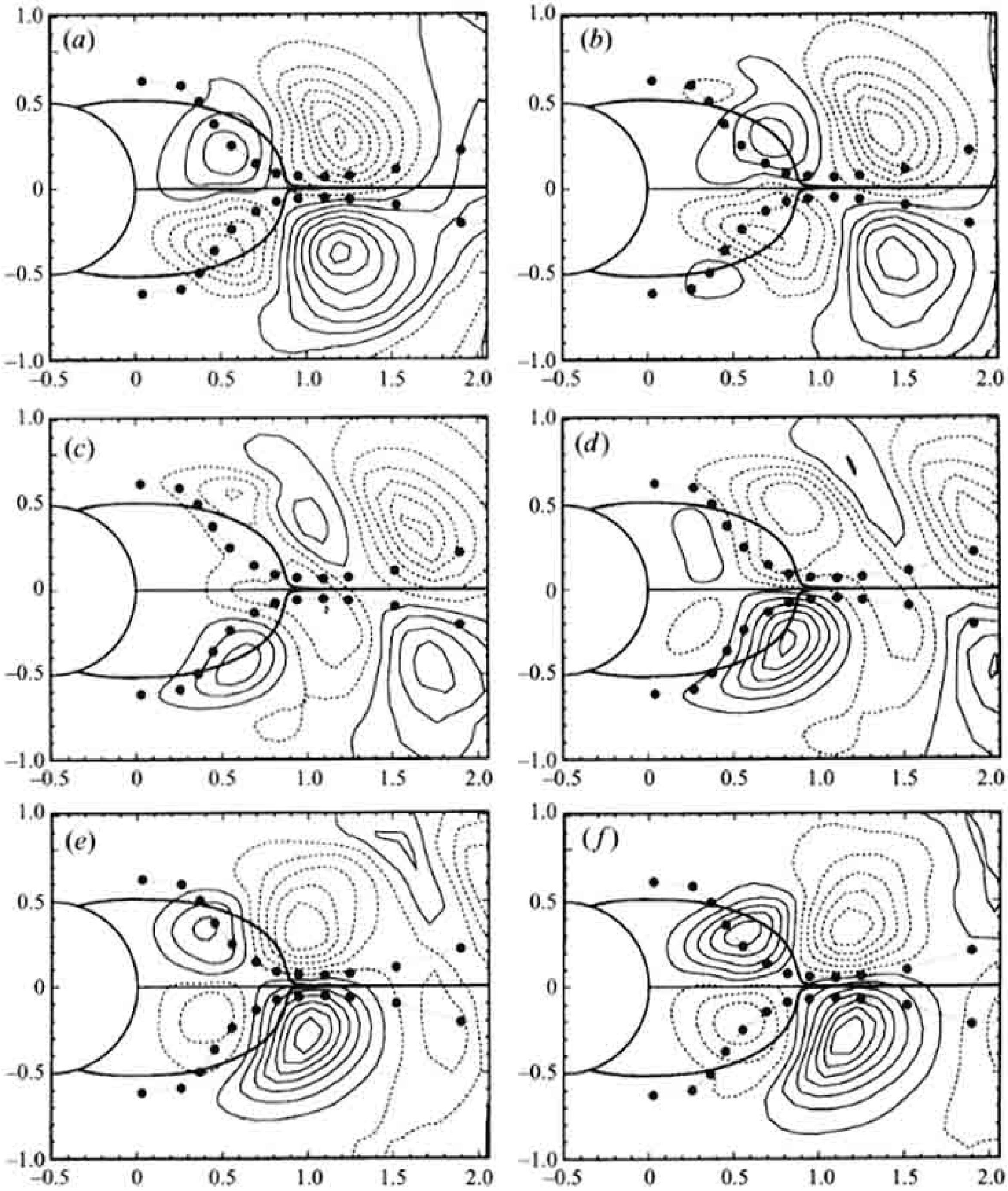

FIGURE 12. Distribution of $\tilde{u}\tilde{v}$ correlation corresponding to the six phase instances shown in figure 9.

as if it has been produced by a single strong vortex located somewhere in the beginning of the Phase II region of the vortex trajectory.

In the preceding discussion, we have shown that the spanwise Kármán vortex in its Phase II regime dictates not only the Reynolds shear stress distribution in the near wake but also the shape and size of the mean recirculation region through the location of the reattachment point. It stands to reason that Reynolds shear stress will change sign in the vicinity of the separating streamline. Therefore, the near-zero value of the coherent Reynolds shear stress distribution along the periphery of the wake is not a mere coincidence. The above line of reasoning can be used to explain the distribution of the coherent contribution to the Reynolds streamwise normal stress as well. Again the primary contribution is when the vortex is at the beginning of Phase II and this relation can be clearly observed in the close resemblance of the distribution of $\tilde{u}$ in figure 11(*a*) and $\overline{u'^2}$ in figure 2(*b*). Similar scenarios of vortex evolution and Reynolds stress distribution have also been observed in the other cylinder and normal-plate geometries. This suggests that our observations regarding the coherent contribution to Reynolds stress distributions along the separating streamlines may be universally applicable, irrespective of the bluff-body geometry and the actual Reynolds number, so long as the Kármán vortices strongly interact in the near-wake region.

## 4. Discussion and conclusions

Table 3 provides a convenient way to compare at a glance the net contribution to the force balance from pressure and Reynolds stress components for the various cases considered in this study. Based on this result, the 10 cases seem to divide into two different sets: the cylinder geometries of circular, elliptic and square cross-sections and the normal flat plate. In the former, the net streamwise force due to normal stress, which is pointed against the flow direction, dominates over the net streamwise force due to the shear stress, which is pointed along the flow direction. As a result the pressure on the leeward side of the body is higher than the pressure along the separating streamline and the net pressure force on the wake bubble is also directed away from the body along the flow direction. On the other hand, in the case of flow around a normal plate the net streamwise force due to the shear stress dominates over the net streamwise force due to normal stress. As a result the pressure on the leeward side of the body is lower than the pressure along the separating streamline and the net pressure force on the wake bubble is also directed against the flow direction.

In all the cases considered the contribution to the force balance from normal stress is significant. The peak value of normal stress coefficient occurs along the separating streamlines somewhere between the separation and reattachment points. This peak value is observed to be around 0.2 uniformly in all the cases, except perhaps for the square cylinder where the experiments of Lyn *et al.* (1995) have measured a peak value of close to 0.3. In contrast the normal stress at the reattachment point ($R_n$) shows considerable variation from case to case as it varies from near zero at low Reynolds numbers to close to the peak value at higher Reynolds numbers. Thus, it appears that the distribution of the total normal stress changes with the bluff-body shape and with Reynolds number. This variation can be understood in terms of the coherent and incoherent contributions. From figures 4 and 7 it can be seen that the incoherent contribution to the normal stress is nearly a constant all along the separating streamlines, except close to the separation points where the normal stress rapidly approaches zero. This gives the plot of $\hat{C}_n$ its characteristic rectangular shape in figures 4 and 7. On the other hand, the coherent contribution to the normal stress reaches its peak a short distance from the separation point and then continuously decreases towards the reattachment point along the separating streamline. This gives the plot of $\tilde{C}_n$ its characteristic triangular shape. Together they explain the change in the shape of the total normal stress distribution with increasing Reynolds number.

The coherent contribution to the normal stress decreases with Reynolds number, possibly due to the weakening of the large-scale vortices at the expense of fluctuations at smaller scales. In the cylinder geometries the incoherent contribution is negligible at lower Reynolds numbers when the shear layers are laminar. But as Reynolds number increases and as the shear layers become unstable, the incoherent contribution to normal stress increases substantially. In the case of the normal flat plate, even at low Reynolds numbers, the incoherent contribution to the normal stress is significant due to the irregular nature of the shedding process arising from the low-frequency oscillation. Interestingly, in the normal-plate geometry the incoherent contribution to the normal stress has remained nearly the same over the Reynolds number range of 250 to 28000 considered in this study. It is not clear if the incoherent contribution to the normal stress will remain at the same level at even higher Reynolds numbers when the shear layers are strongly turbulent.

As shown in §3.5 the coherent Reynolds shear stress is in general so small all along the periphery of the mean recirculation region that it can be reasonably neglected in the force balance. In the cylinder geometries, the incoherent contribution to the shear stress is small at low Reynolds numbers. From figure 4 it can be seen that as transition moves upstream into the shear layers the incoherent contribution to shear stress increases. The shear stress coefficient is constrained to be zero along the wake centreline, but in all the three cases, $Re = 3900$, 21400 and 140000, $\hat{C}_\tau$ quickly reaches a value of approximately 0.05 near the reattachment point. At $Re = 3900$ the shear stress remains appreciable only in the downstream half of the separating streamline and is nearly zero in the upstream half. At $Re = 140000$, however, the transition point would have moved upstream closer to the separation point and accordingly the experimental data suggest that $\hat{C}_\tau$ remains significant all along the separating streamline and slowly approaches zero at the separation point.

In the case of a normal plate, the coherent part of the shear stress still makes a smaller contribution than the incoherent part. The presence of a non-zero incoherent contribution to shear stress even at $Re = 250$ can be attributed to the irregular vortex shedding. Oscillations in the wake at a low frequency in addition to the primary shedding frequency accounts for the significantly higher $\hat{C}_\tau$ measured for the $Re = 28000$ normal plate than the corresponding cylinder cases. Therefore, the total shear stress distribution around the mean wake bubble of a normal plate is systematically higher than in the cylinder geometries. For example, at high Reynolds numbers the maximum $C_\tau \approx 0.1$ for the normal plate is nearly twice as large as the corresponding maximum value of $C_\tau \approx 0.06$ for the cylinder. This increased level of shear stress in a normal plate, along with the somewhat longer wake, results in a net shear force larger than that due to normal stresses, thus explaining the fundamental difference in the direction of the pressure force.

Even though the origin of the irregular shedding mechanism in the case of the normal plate is not yet completely resolved and is under investigation (Najjar & Balachandar 1997), its dominant role in the normal plate underscores the importance of the shape of the bluff-body geometry in determining its drag and lift forces. The presence of an afterbody downstream of the separating point seems to play an important role in stabilizing the shear layers and in mitigating any low-frequency oscillation at low Reynolds numbers. For example, the normal plate and square cylinder are similar in many respects in terms of the fixed separation points at the front corners and the characteristics of the separating streamline leaving the surface. However, the presence of an afterbody in a square cylinder seems to alter the shear layer dynamics, the roll-up process and the large-scale vortex dynamics. In this regard a future systematic study ranging from a normal plate to square and rectangular cylinders will be useful.

For modelling purposes it is desirable to seek a universal value for the streamwise normal and shear stresses along the separating streamlines. The average streamwise normal and shear stresses, defined as $\langle C_n \rangle = [C_n] D/H$ and $\langle C_\tau \rangle = [C_\tau] D/L$, are plotted in figure 13 against the universal Reynolds number, $2HU_e/\nu$, for all the cases considered. The tendency towards a universal value can be observed at higher

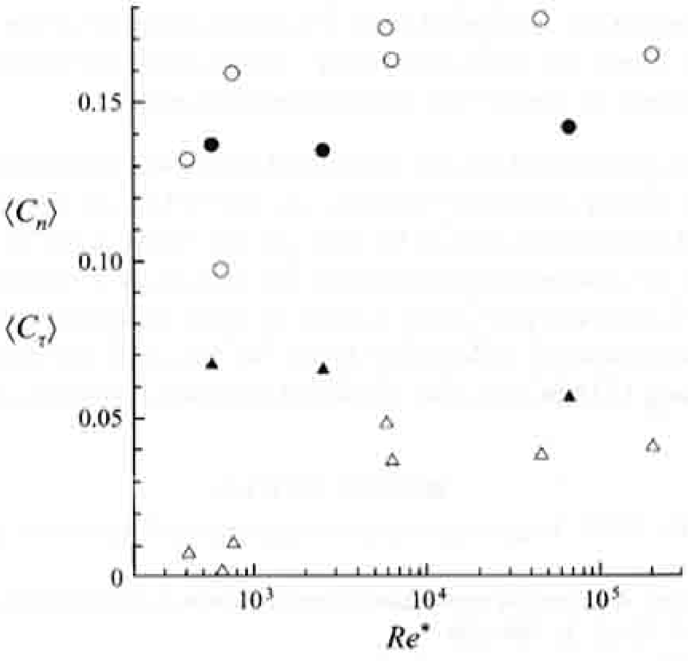

FIGURE 13. Average streamwise normal and shear stress coefficients plotted against the universal Reynolds number based on wake thickness and shear layer velocity for the different cases. ○, $\langle C_n \rangle$ for cylinder geometry; ●, $\langle C_n \rangle$ for normal-plate geometry; △, $\langle C_\tau \rangle$ for cylinder geometry; ▲, $\langle C_\tau \rangle$ for normal-plate geometry.

Reynolds numbers. At the higher end of the Reynolds number range considered, $\langle C_n \rangle$ approaches a value of 0.16 and 0.14 for the cylinder and normal-plate geometries considered and $\langle C_\tau \rangle$ approaches a value of 0.04 and 0.055, respectively. It must be cautioned that the Reynolds number range considered covers only the laminar and transitional wakes and that the attached boundary layer remains laminar even in the case of a circular cylinder at $Re = 140000$. From figure 13 it is not completely clear if the observed difference between the cylinder and normal-plate geometries will exist at even higher Reynolds numbers when the separation is fully turbulent. The asymptotic values of 0.16 and 0.14 for the average normal stress coefficients are lower than the corresponding peak value of approximately 0.29 measured along the centreline of a canonical free shear layer by Liepmann & Laufer (1947). However their measured value along the dividing streamline ranges from 0.14 to 0.17 sufficiently downstream, which compare favourably with the present estimate. On the other hand, the average shear stress coefficient for both the cylinder and normal-plate geometries is nearly twice as large as the canonical value of 0.025 quoted by Roshko (1993*b*) based on the experimental results of Liepmann & Laufer (1947).

Based on the above asymptotic values of $\langle C_n \rangle$ and $\langle C_\tau \rangle$, an estimate for the difference in average pressure coefficient between the leeward side of the bluff body and the separating streamline applicable at high Reynolds number can be written as $(0.04L/H - 0.16)$ and $(0.055L/H - 0.14)$ for the cylinder and normal-plate geometries respectively. In the context of pressure measurement along the wake centreline, the above formulae can be considered as an estimate for the pressure recovery coefficient at the reattachment point. For the $Re = 3900$ circular cylinder case, $\langle C_p \rangle = -0.019$, directly obtained from the computational results compares reasonably well with an estimate of $\langle C_p \rangle_{est} = -0.026$ obtained using $L = 1.99$ and $H = 0.6$ (see table 2). Comparisons with the results of lower Reynolds number simulations are not so good, owing to the asymptotic nature of the formulae and to the increasing contribution from viscous stresses to the force balance. In order to further verify the above estimates, pressure measurements are needed at high Reynolds numbers over different bluff-body geometries, at least along the wake centreline. Also needed are simultaneous streamwise velocity measurements to locate the reattachment point.

The different computational results presented here have been performed on the Cray C90 at Pittsburgh Supercomputer Center, on the CM5 at the National Center for Supercomputing Applications (NCSA) and on the Cray C90 at NASA–Ames. The authors would like to acknowledge sincerely Professors B. Cantwell, A. Krothappalli, D. A. Lyn and A. Leder for providing access to their experimental data. F.M.N. was supported by a postdoctoral fellowship from NCSA and the Division of Advanced Scientific Computing (DASC) at the National Science Foundation.

## REFERENCES

Arie, M. & Rouse, H. 1956 Experiments on two-dimensional flow over a normal wall. *J. Fluid Mech.* **1**, 129.

Batchelor, G. K. 1956 A proposal concerning laminar wakes behind bluff bodies at large Reynolds numbers. *J. Fluid Mech.* **1**, 388–398.

Bloor, S. M. 1964 The translation to turbulence in the wake of a circular cylinder. *J. Fluid Mech.* **19**, 290–304.

Cantwell, B. & Coles, D. 1983 An experimental study of entrainment and transport in the turbulent near wake of a circular cylinder. *J. Fluid Mech.* **136**, 321.

Canuto, C., Hussaini, M. Y., Quarteroni, A. & Zang, T. A. 1988 *Spectral Methods in Fluid Dynamics.* Springer.

Carrière, P. & Sirieix, M. 1960 Facteurs d'influence du recollement d'un écoulement supersonique. *Proc. 10th Intl Congr. Appl. Mech. Stresa, Italy* p. 205.

Castro, I. P. & Haque, A. 1987 The structure of a turbulent shear layer bounding a separation region. *J. Fluid Mech.* **179**, 439.

Chapman, D. R., Kuehn, D. M. & Larson, H. K. 1957 Investigation of separated flow in supersonic and subsonic streams with emphasis on the effect of transition. *NACA Rep.* 1356.

Chong, M. S., Perry, A. E. & Cantwell, B. J. 1990 A general classification of three-dimensional flow fields. *Phys. Fluids* A **5**, 765–777.

Dallmann, U., Hilgenstock, A., Riedelbauch, S., Schulte-Werning, B. & Vollmers, H. 1991 On the footprints of three-dimensional separated vortex flows around blunt bodies. *AGARD CP*-494.

Durão, D. F. G., Heitor, M. V. & Perira, J. C. F. 1986 A laser anemometry study of separated flow around a squared obstacle. In *Laser Anemometry in Fluid Mechanics III* (ed. R. J. Adrian *et al.*). LADOAN-IST, Lisbon, Portugal.

Durão, D. F. G., Heitor, M. V. & Perira, J. C. F. 1988 Measurements of turbulent and periodic flows around a square cross-section cylinder. *Exps. Fluids.* **6**, 298–304.

Fornberg, B. 1980 A numerical study of steady viscous flow past a circular cylinder. *J. Fluid Mech.* **98**, 819–855.

Gerrard, J. H. 1978 The wakes of cylindrical bluff body at low Reynolds number. *Phil. Trans. R. Soc. Lond.* A **288**, 351–382.

Hayakawa, M. & Hussain, F. 1989 Three-dimensionality of organized structures in a plane turbulent wake. *J. Fluid Mech.* **206**, 375–404.

Kirchhoff, G. 1869 Zur Theorie freier. *Flüssigkeitsstrahlen* **70**, 416.

Korst, H. H. 1956 A theory for base pressure in transonic and supersonic flows. *J. Appl. Mech.* **23**, 593.

Leder, A. 1991 Dynamics of fluid mixing in separated flows. *Phys. Fluids* A **3**, 1741.

Liepmann, H. W. & Laufer, J. 1947 Investigation of free turbulent mixing. *NACA TN* 1257.

Lighthill, M. J. 1945 A note on cusped cavities. *Aeronaut. Res. Counc. Rep. and Memo.* 2328.

Lisoski, D. 1993 Nominally two-dimensional flow about a normal flat plate. PhD thesis, California Institute of Technology, Pasadena, California.

LYN, D. A., EINAV, S., RODI, W. & PARK, J. H. 1995 A laser-Doppler velocimetry study of ensemble-averaged characteristic of the turbulent near wake of a square cylinder. *J. Fluid Mech.* **304**, 285–319.

LYN, D. A. & RODI, W. 1994 The flapping shear layer formed by flow separation from the forward corner of a square cylinder. *J. Fluid Mech.* **267**, 353–376.

MITTAL, R. 1995 Study of flow past elliptic and circular cylinders using direct numerical simulation, PhD thesis, University of Illinois, Urbana–Champaign.

MITTAL, R. 1996 Progress in large-eddy simulation of flow past a circular cylinder. *CTR Ann. Res. Briefs*, pp. 233–242. Stanford University.

MITTAL, R. & BALACHANDAR, S. 1995*a* Effect of three-dimensionality on the lift and drag of nominally two-dimensional cylinders. *Phys. Fluids* **7**, 1841–1865.

MITTAL, R. & BALACHANDAR, S. 1995*b* Generation of streamwise vortical structures in bluff body wakes. *Phys. Rev. Lett.* **75**, 1300–1303.

MITTAL, R. & BALACHANDAR, S. 1996 Direct numerical simulation of flow past elliptic cylinders. *J. Comput. Phys.* **124**, 351–367.

MITTAL, R. & BALACHANDAR, S. 1997 On the inclusion of three-dimensional effects in the simulation of two-dimensional bluff-body wake flows. *1997 ASME Fluid Engng Div. Summer Meeting, Vancouver.*

NAJJAR, F. M. 1994 Direct numerical simulations of separated and separated-reattaching flows on massively parallel processing computers. PhD thesis, University of Illinois, Urbana–Champaign.

NAJJAR, F. M. & BALACHANDAR, S. 1997 Low-frequency unsteadiness in the wake of a normal flat plate. *J. Fluid Mech.* (submitted).

NAJJAR, F. M. & VANKA, S. P. 1995 Effects of intrinsic three-dimensionality on the drag characteristics of a normal flat plate. *Phys. Fluids* **7**, 2516–2518.

NASH, J. F. 1963 An analysis of two-dimensional turbulent base flow, including the effect of the approaching boundary layer. *ARC R&M* 3344.

NISHIOKA, M. & SATO, H. 1978 Mechanism of determination of the shedding frequency of vortices behind a cylinder at low Reynolds numbers. *J. Fluid Mech.* **89**, 49–60.

PERRY, A. E. & STEINER, T. R. 1987 Large scale vortex structures in turbulent wakes behind bluff bodies. Part 1. Vortex formation process. *J. Fluid Mech.* **174**, 233–270.

REYNOLDS, W. C. & HUSSAIN, A. K. M. F. 1972 The mechanics of an organized wave in turbulent shear flow. Part 3. Theoretical models and comparisons with experiments. *J. Fluid Mech.* **54**, 263.

RIABOUCHINSKY, D. 1920 On steady fluid motion with free surfaces. *Proc. Lond. Math. Soc.* (2) **19**, 206.

ROBERTS, J. B. 1966 On the prediction of base pressure in two-dimensional supersonic turbulent flow. *ARC R&M* 3434.

ROSHKO, A. 1954 A new hodograph for free streamline theory. *NACA TN* 3168.

ROSHKO, A. 1993*a* Perspectives on bluff body aerodynamics. *J. Wind Engng Ind. Aerodyn.* **49**, 79.

ROSHKO, A. 1993*b* Free shear layers, base pressure and bluff-body drag. In *Proc. Symp. on Developments in Fluid Dynamics and Aerospace Engineering, Bangalore, India.*

ROSHKO, A. & FISZDON, W. 1969 On the persistence of transition in the near wake. In *Problems of Hydrodynamics and Continuum Mechanics*, p. 606. Soc. Industrial and Appl. Math., Philadelphia.

ROSHKO, A. & LAU, J. C. 1965 Some observations on transition and reattachment of a free shear layer in incompressible flow. In *Proc. 1965 Heat Transfer and Fluid Mechanics Inst.* (ed. A. F. Charwat), p. 157. University of California, Los Angeles.

SYCHEV, V. V. 1982 Asymptotic theory of separated flows. *Mekh. Zhid. i Gaza* **2**, 20.

TANNER, M. 1973 Theoretical prediction of base pressure for steady base flow. *Prog. Aerospace Sci.* **14**, 177.

WIESELSBERGER, C. 1922 New data on the laws of fluid resistance. *NACA TN* 84.

WILLIAMSON, C. H. K. 1996 Vortex dynamics in the cylinder wake. *Ann. Rev. Fluid Mech.* **28**, 477.

WU, T. Y. 1962 A wake model for free-streamline flow theory. Part 1. Fully and partially developed wake flows and cavity flows past an oblique flat plate. *J. Fluid Mech.* **13**, 161–181.

WU, T. Y. 1972 Cavity and wake flows. *Ann. Rev. Fluid Mech.* **4**, 243–284.